The preparation and characterization of bismuth thin films on GaSb(110) using low energy electron diffraction

by Scott Len Lantz

A thesis submitted in partial fulfillment of the requirements for the degree of Master of Science in Physics
Montana State University

Abstract:
The growth of thin bismuth films on the GaSb(110) surface has been studied using low energy electron diffraction (LEED) and Auger electron spectroscopy (AES). The GaSb samples were single crystal bars and the (110) surface was prepared by cleaving in situ. Bismuth was evaporated from a solid source, and the evaporation was monitored with a quartz crystal oscillator. Diffraction spot profiles and integrated intensity versus voltage (IV) curves were measured at temperatures ranging from 120 K to 350 C. Bismuth was found to grow epitaxially for monolayer coverages, preserving the p(lxl) LEED pattern symmetry. Upon annealing a phase transition occurred such that the p(lxl) symmetry was replaced by a p(lx2) symmetry, where the LEED pattern periodicity was doubled along the [001] direction of the bulk GaSb crystal. Preliminary work has been done toward the determination of the atomic structure of the Bi/GaSb(110) interface. Modifications were made to the existing computer programs, including the incorporation of the simplex algorithm into the structure search decision-making process. Using this method, the calculated atomic structure of the clean GaSb(110) surface was shown to be in agreement with that obtained by previous methods. Searches were also made for the atomic structure of the p(lxl) structure for a bismuth coverage of one monolayer. The results indicate an ordered bismuth overlayer with an atomic structure differing markedly from the truncated bulk or reconstructed clean GaSb(110) surface structure.

THE PREPARATION AND CHARACTERIZATION OF BISMUTH THIN FILMS ON GaSb(110) USING LOW ENERGY ELECTRON DIFFRACTION

by

Scott Len Lantz

A thesis submitted in partial fulfillment
of the requirements for the degree

of

Master of Science

in

Physics

MONTANA STATE UNIVERSITY
Bozeman, Montana

March 1990

APPROVAL

of a thesis submitted by

Scott Len Lantz

This thesis has been read by each member of the thesis committee and has been found to be satisfactory regarding content, English usage, format, citations, bibliographic style, and consistency, and is ready for submission to the College of Graduate Studies.

23 March 90
Date

Chairperson, Graduate Committee

Approved for the Major Department

23 March 90
Date

Head, Major Department

Approved for the College of Graduate Studies

April 4, 1990
Date

Graduate Dean

STATEMENT OF PERMISSION TO USE

In presenting this thesis in partial fulfillment of the requirements for a master's degree at Montana State University, I agree that the Library shall make it available to borrowers under rules of the Library. Brief quotations from this thesis are allowable without special permission, provided that accurate acknowledgment of source is made.

Permission for extensive quotation from or reproduction of this thesis may be granted by my major professor, or in his absence, by the Dean of Libraries when, in the opinion of either, the proposed use of the material is for scholarly purposes. Any copying or use of the material in this thesis for financial gain shall not be allowed without my written permission.

Signature Scott LaLonde

Date 3-23-90

TABLE OF CONTENTS

LIST OF FIGURES

LIST OF FIGURES-continued

ABSTRACT

The growth of thin bismuth films on the GaSb(110) surface has been studied using low energy electron diffraction (LEED) and Auger electron spectroscopy (AES). The GaSb samples were single crystal bars and the (110) surface was prepared by cleaving *in situ*. Bismuth was evaporated from a solid source, and the evaporation was monitored with a quartz crystal oscillator. Diffraction spot profiles and integrated intensity versus voltage (IV) curves were measured at temperatures ranging from 120 K to 350 C. Bismuth was found to grow epitaxially for monolayer coverages, preserving the p(1x1) LEED pattern symmetry. Upon annealing a phase transition occurred such that the p(1x1) symmetry was replaced by a p(1x2) symmetry, where the LEED pattern periodicity was doubled along the [001] direction of the bulk GaSb crystal. Preliminary work has been done toward the determination of the atomic structure of the Bi/GaSb(110) interface. Modifications were made to the existing computer programs, including the incorporation of the *simplex algorithm* into the structure search decision-making process. Using this method, the calculated atomic structure of the clean GaSb(110) surface was shown to be in agreement with that obtained by previous methods. Searches were also made for the atomic structure of the p(1x1) structure for a bismuth coverage of one monolayer. The results indicate an ordered bismuth overlayer with an atomic structure differing markedly from the truncated bulk or reconstructed clean GaSb(110) surface structure.

CHAPTER 1

INTRODUCTION

The work presented in this thesis represents the results of the experimental and theoretical investigations into the growth of thin bismuth films on the GaSb(110) surface. The motivation for such a study is many-fold. GaSb (gallium antimonide) is an important III-V semiconductor. It has many industrial applications for the construction of electronic devices such as electro-optical sensors and light emitting diodes [1]. The successful construction of electronic devices, which are getting increasingly smaller, could benefit greatly from the knowledge of atomic and electronic structures of semiconductor-metal interfaces. This is important in studying the formation of Schottky barriers and ohmic contacts [2]. At the atomic scale, however, little is understood about the electronic structure at these interfaces, due to complex atomic reconstructions of the semiconductor substrate and lack of sufficient theoretical models to describe the interface [2]. Although the (110) surface of the III-V semiconductors is less used in industrial applications (than, for example the (100) surface), it is somewhat simpler in that the surface is charge-neutral, and the substrate reconstructions are comparatively well understood [2,3]. Clean (110) surfaces hence provide an excellent basis for the study of atomic and electronic structures at metal interfaces.

Bismuth was selected as an absorbate because it was found to form an ordered interface on a similar III-V compound GaAs(110) [4]. For this reason it

was believed that bismuth would form an ordered interface on GaSb(110), which could then be studied by LEED (low energy electron diffraction), which is a powerful and extensively-used tool for surface analysis.

The experimental techniques used in the study of the Bi/GaSb(110) system include LEED and AES (Auger electron spectroscopy). The growth of bismuth was investigated for monolayer coverages, and the effects of annealing were studied. Measurements taken with LEED included diffraction spot intensity profiles and intensity versus voltage (IV) curves. Auger measurements were primarily used to measure the desorption of bismuth that occurred when the sample was annealed.

The theoretical analysis of the data involved modelling of the atomic structure of the interface. This included dynamical LEED calculations for the generation of IV data for the proposed model, which could then be compared to the experimental IV data. A best fit structural model was then searched for by making changes to the model until the calculated data best matched the experimental data. In the following chapters, the results of these studies of the Bi/GaSb(110) system are presented following a description of the techniques used.

CHAPTER 2

CONCEPTS IN LEED CRYSTALLOGRAPHY

The LEED Experiment

The essential elements of a LEED apparatus consist of an ultra-high vacuum chamber, an electron gun to provide a monoenergetic electron beam over an energy range from 30 to 400 eV, a crystal holder with facilities for moving, heating and cooling the sample, and a detection system for measuring the number of elastically scattered electrons in a prescribed direction. The type of detection system used in this work is the display system shown schematically in Figure 1.

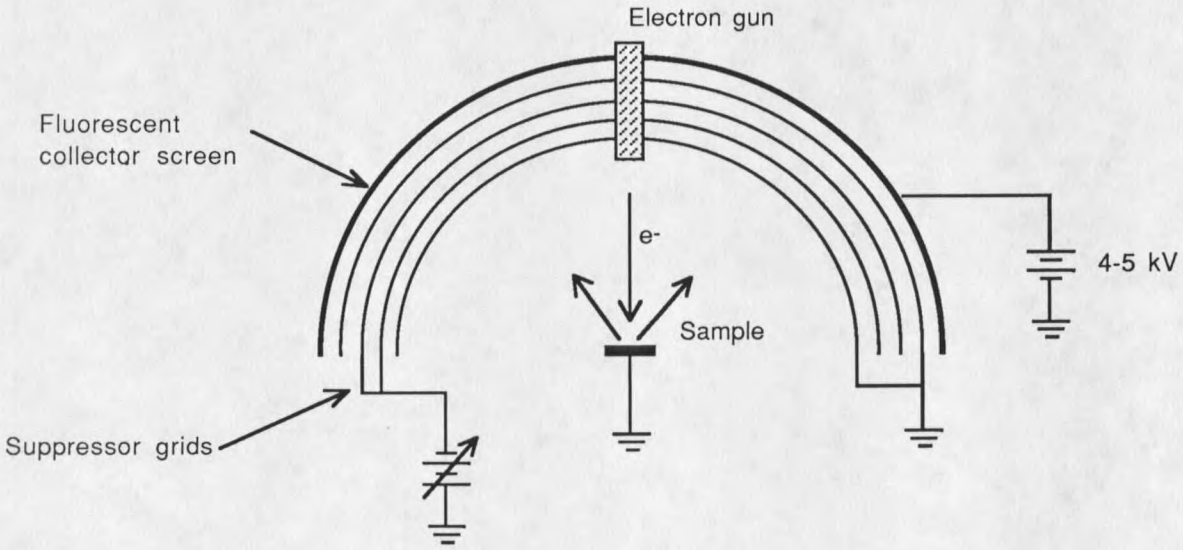

Figure 1: Display detection system for LEED

The electron gun produces a beam of electrons which scatter from the crystal surface. The elastically scattered electrons are filtered by the suppressor grids, then accelerated into the fluorescent screen by a voltage of 4-5 kV. The intensity pattern produced by the electrons striking the screen can then be measured by photographic or video recording techniques. For a well-ordered crystal surface, the LEED intensity pattern contains a wealth of information concerning the surface symmetries and surface atomic geometries. The extraction of these surface properties, though, often requires extensive analyses. The notation and methods used in such analyses are developed below.

Surface Classifications

When considering an ordered surface, there are two important fundamental concepts, that of a lattice and a basis. The lattice is the two dimensional array of reference points which possess the translational symmetries of the surface. The basis is the arrangement of the surface atoms with respect to the lattice points. The geometry of a particular surface structure is said to be completely determined once both the lattice and the basis are known. There are five possible distinct two dimensional lattices, called Bravais lattices. These are shown in Figure 2. The primitive vectors, $\mathbf{a}_1$ and $\mathbf{a}_2$, define the surface unit cell, and are generally selected to form the smallest possible parallelogram which preserves the surface symmetries.

The classification of a surface structure often relates the two dimensional surface lattice to the three dimensional substrate lattice. One scheme, proposed by Park and Madden [5], relates the surface lattice primitive vectors ($\mathbf{a}_1$,$\mathbf{a}_2$) to

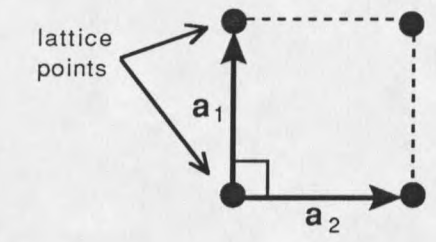

Square

$a_1 = a_2$

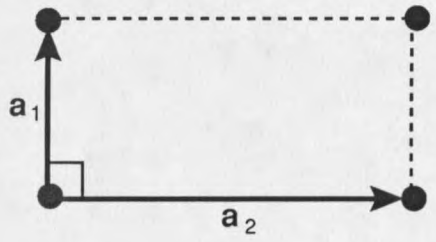

Primitive Rectangular

$a_1 \neq a_2$

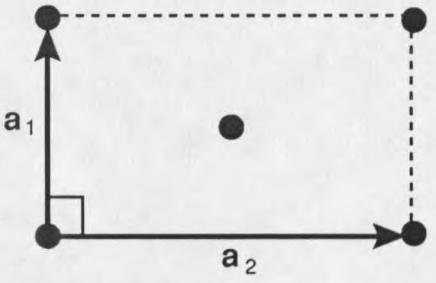

Centered Rectangular

$a_1 \neq a_2$

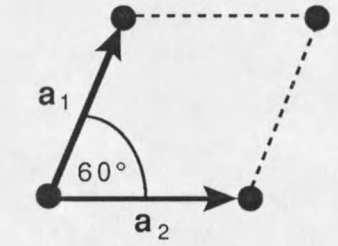

Hexagonal

$a_1 = a_2$

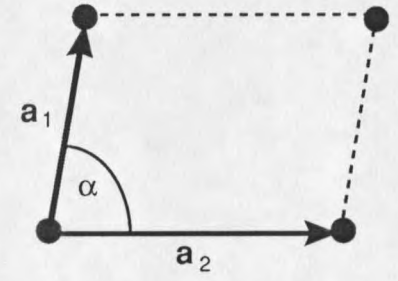

Oblique

$a_1 \neq a_2$

$\alpha \neq 90°$

Figure 2: Two-dimensional Bravais lattices

those of a parallel substrate plane ($\mathbf{b}_1$,$\mathbf{b}_2$) with a transformation matrix **M**, such that

$$\begin{aligned} \mathbf{b}_1 &= M_{11}\mathbf{a}_1 + M_{12}\mathbf{a}_2 \\ \mathbf{b}_2 &= M_{21}\mathbf{a}_1 + M_{22}\mathbf{a}_2 \end{aligned} \tag{1}$$

The structure is called simple when all entries of **M** are integers, and coincidental if **M** contains both integers and rational numbers. If **M** contains irrational numbers, the structure is labelled incoherent or incommensurate. Although universally applicable, this method does not always provide an intuitive picture for what the structure looks like. Other methods have been proposed which are more descriptive, such as the one proposed by Wood [6]. Here, the relation between the surface and substrate lattices is expressed by the ratios of the lengths of the primitive vectors, $|\mathbf{b}_1/\mathbf{a}_1|$ and $|\mathbf{b}_2/\mathbf{a}_2|$, and the rotation angle between the two lattices, φ. The surface unit cell is labelled as either centered (c), or primitive (p). A centered unit cell implies that there is a lattice point in the center of the surface unit cell. This method is simple and applicable to a large number of structures, including the Bi/GaSb(110) system studied here. Some examples of labelling with this scheme are presented in Figure 3.

Directions on the surface are usually expressed in relation to the unit cell. A standard approach is to use the Miller indices h' and k', where h' and k' are both integers, such that (h',k') refers to a direction on the surface. This direction is defined to be perpendicular to the translation vector **D** given by

$$\mathbf{D} = h'\mathbf{a}_1 + k'\mathbf{a}_2 \tag{2}$$

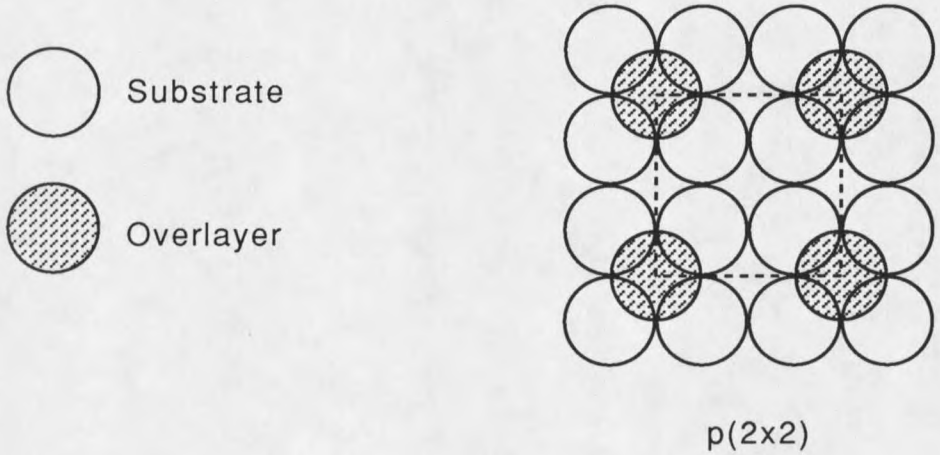

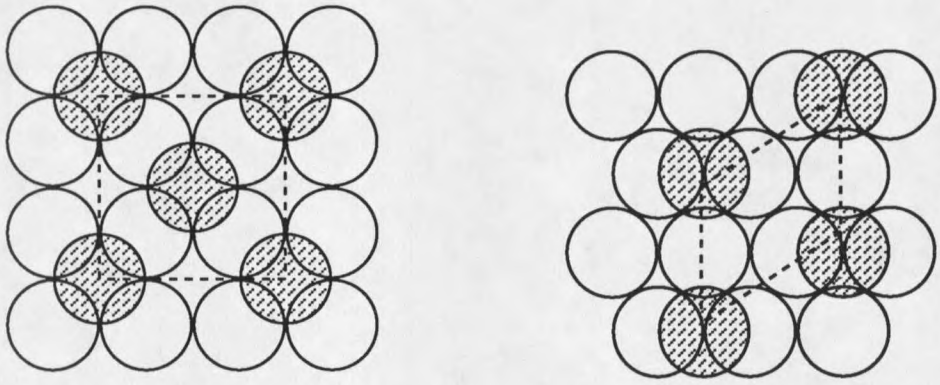

Figure 3: Examples of surface classifications

As illustrated in Figure 4, the surface lattice can be thought of as parallel rows of points with separation $d_{h'k'}$ given by

$$\frac{1}{d_{h'k'}^2} = \frac{h'^2}{a_1^2 \sin^2\gamma} + \frac{k'^2}{a_2^2 \sin^2\gamma} - \frac{2h'k'\cos\gamma}{a_1 a_2 \sin^2\gamma} \tag{3}$$

where γ is the angle between $\mathbf{a}_1$ and $\mathbf{a}_2$. This interpretation will become useful in the next section in discussing the geometric theory of diffraction.

Geometric Theory of Diffraction

The starting point for describing electron diffraction at crystal surfaces is the de Broglie relation,

$$\lambda = h/p \tag{4}$$

which relates the linear momentum of the electron p to its wavelength λ. h is Planck's constant (4.13×10^{-15} eV sec). When expressed in terms of the kinetic energy of the electron ($E = p^2/2m$), the de Broglie relation becomes

$$\lambda = h/\sqrt{2mE} \tag{5}$$

When λ is in Angstroms (Å), and the energy E is in electron volts (eV), the relation is approximately,

$$\lambda \cong \sqrt{150/E} \tag{6}$$

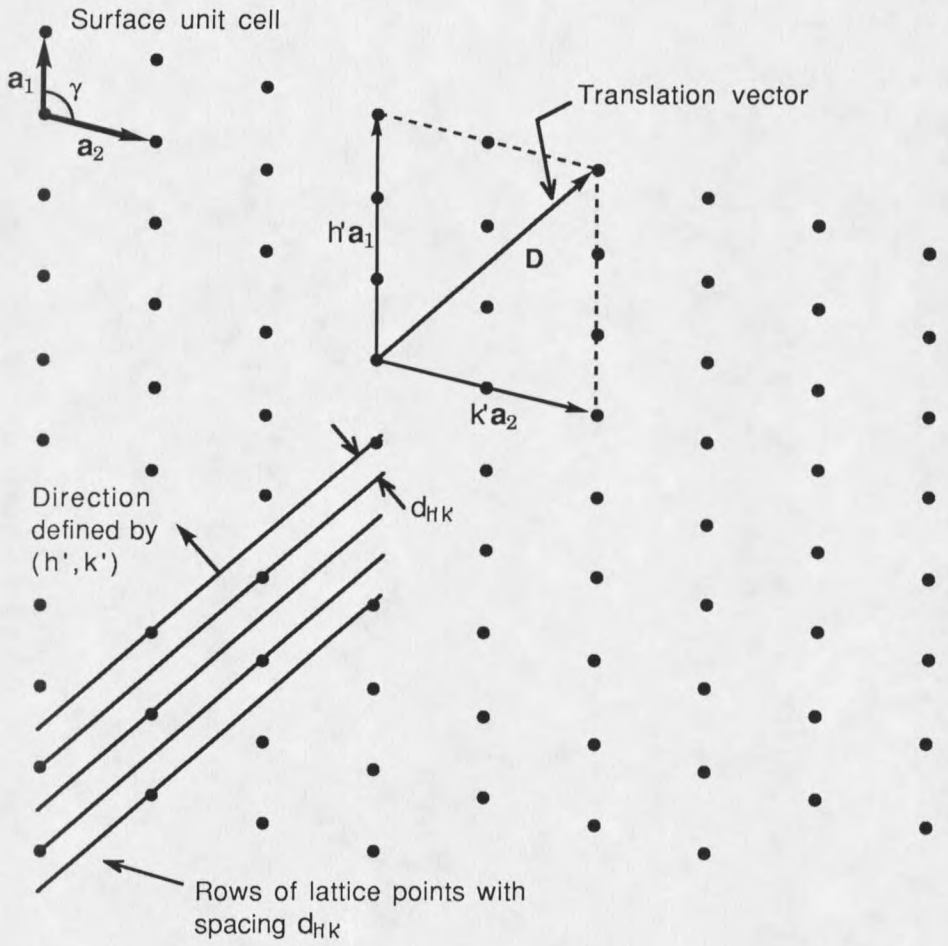

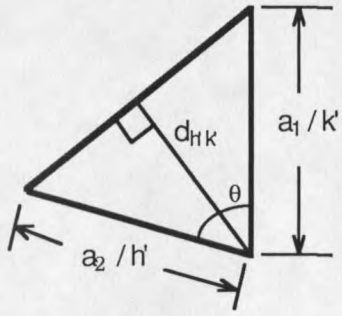

$$\theta = \pi - \gamma$$

$$\frac{1}{d_{HK}^2} = \frac{h'^2}{a_1^2 \sin^2\gamma} + \frac{k'^2}{a_2^2 \sin^2\gamma} - \frac{2h'k'\cos\gamma}{a_1 a_2 \sin^2\gamma}$$

Figure 4: Row representation of surface lattice points

Interference effects occur when the electron wavelength is of the same order of magnitude as the atomic spacing on the crystal surface. With atomic spacings on the order of a few Angstroms, the corresponding energy range is 1 to 500 eV. The actual energy range used in LEED experiments is somewhat smaller, 50-300 eV, owing to inelastic scattering and instrumental effects, which are discussed in later sections. In the geometric theory, all scattering is assumed to be elastic, and instrumental effects are ignored.

For elastic wave scattering from a one dimensional periodic array, constructive interference takes place when the scattered waves from neighboring lattice points have path differences of multiples of the electron wavelength λ. If d is the array spacing, and θ_0 is the angle of incidence measured from the normal, then constructive interference of the back-scattered waves occurs at angles θ when,

$$d(\sin\theta - \sin\theta_0) = n\,\lambda \qquad (7)$$

Here n is an integer denoting the order of diffraction. This is known as the Bragg equation in one dimension. Since our LEED experiments are performed at normal incidence, it will be assumed that $\theta_0 = 0$, henceforth.

In extending the Bragg equation to a two dimensional surface, recall from the previous section that the surface lattice points can be thought of as an ensemble of parallel rows with direction (h',k') and separation $d_{h'k'}$. When each row is considered a scatterer, interference maxima are expected for

$$\sin\theta = (1/d_{h'k'})\,n\,\lambda \qquad (8)$$

or with the use of equation (6),

$$\sin\theta = (1/d_{h'k'}) \cdot n \cdot \sqrt{150/E} \qquad (9)$$

From this equation, it is evident that an increase in electron energy will cause the diffraction maxima to move closer to the surface normal, and that the larger the unit cell, the closer the first maximum will be to the surface normal.

In labelling the diffraction maxima, the Miller indices are combined with the order of diffraction n, to yield the Laue indices,

$$h = n\,h' \qquad \text{and} \qquad k = n\,k' \qquad (10)$$

With this notation, a diffraction maximum is referred to as the (h,k) beam.

With most LEED apparatus, the diffraction beam pattern is directly observable, which in principle allows for the determination of $d_{h'k'}$ and consequently the geometry of the surface unit cell. A more sophisticated approach to analyzing and interpreting LEED patterns makes use of the reciprocal lattice, described below.

For every two dimensional Bravais lattice, there exists a corresponding reciprocal lattice whose primitive vectors, $(\mathbf{a}_1^*, \mathbf{a}_2^*)$ satisfy

$$\mathbf{a}_i \cdot \mathbf{a}_j^* = 2\pi\delta_{ij} \qquad (11)$$

From this equation, the lengths and directions of the reciprocal lattice vectors can be determined.

$$a_i^* = \frac{2\pi}{a_i \sin\gamma} \quad \text{and} \tag{12}$$

$$\mathbf{a}_i^* \perp \mathbf{a}_j \quad \text{for} \quad i \neq j \tag{13}$$

Here again γ is the angle between $\mathbf{a}_1$ and $\mathbf{a}_2$. Reciprocal lattices for the five two dimensional Bravais lattices are shown in Figure 5. The utility of reciprocal space analyses is that the LEED pattern is a direct representation of the reciprocal lattice, as shown below.

The formation of the LEED pattern can be explained using the concept of reciprocal space with the help of an Ewald construction, shown for normal incidence in Figure 6. A set of lines is drawn perpendicular to the surface through the reciprocal lattice points, which become the reciprocal lattice rods. A sphere of radius $1/\lambda$ is then drawn directly above one of the reciprocal lattice points at a distance $1/\lambda$ from the surface. An arrow drawn from the center of the sphere to the surface represents the incident electron wave vector. The intersections of the reciprocal lattice rods with the sphere define the directions of the diffraction beams. The vectors $\mathbf{k}_0$ and $\mathbf{k}$ represent the wave vectors of the incident and scattered beams, respectively, and $\mathbf{k} - \mathbf{k}_0$ is the momentum transfer. It can be seen from this construction that the diffraction beams completely characterize the symmetries of the reciprocal lattice, so the LEED pattern is a direct representation of the lattice.

Once the reciprocal lattice of a surface structure is determined (from the LEED pattern), the Bravais lattice can be found by a transformation from

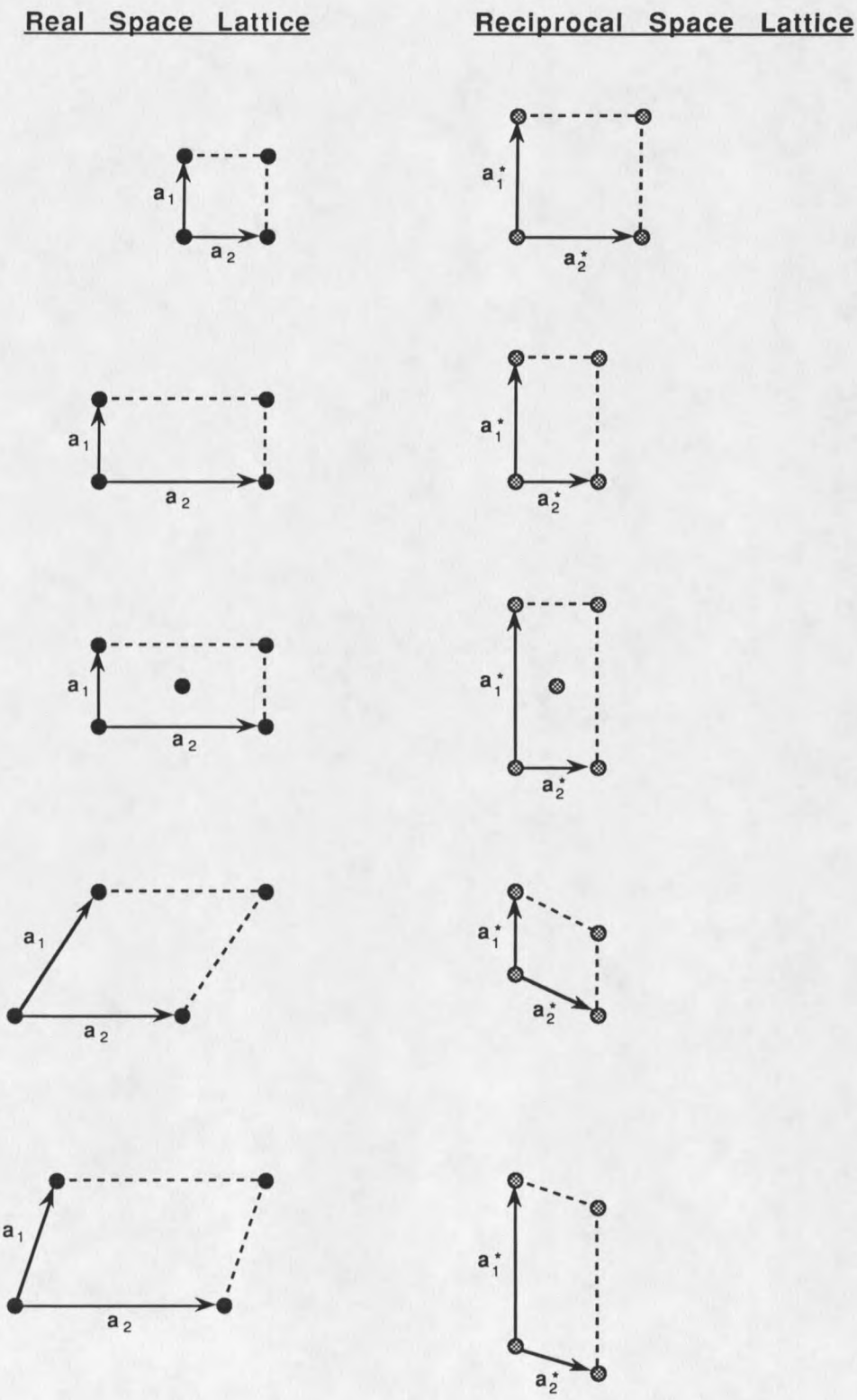

Figure 5: Two-dimensional reciprocal lattices

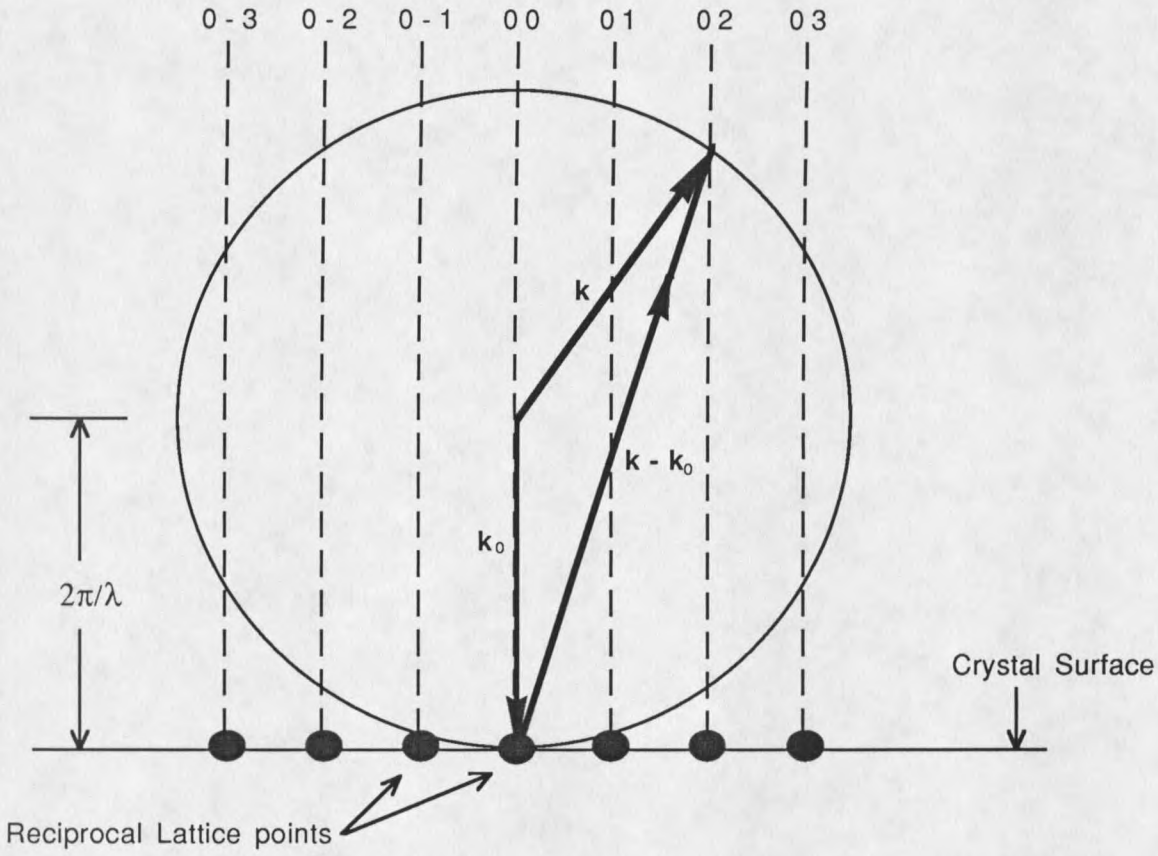

Figure 6: Ewald Construction

reciprocal space to real space. The surface reciprocal lattice, ($\mathbf{a}_1^*$,$\mathbf{a}_2^*$) may be correlated to that of the substrate, ($\mathbf{b}_1^*$,$\mathbf{b}_2^*$) in a manner similar to equation (1).

$$\begin{aligned} \mathbf{b}_1^* &= M_{11}^* \mathbf{a}_1^* + M_{12}^* \mathbf{a}_2^* \\ \mathbf{b}_2^* &= M_{21}^* \mathbf{a}_1^* + M_{22}^* \mathbf{a}_2^* \end{aligned} \tag{14}$$

The M_{ij}^* can be determined by an inspection of the LEED pattern. The transformation to find the matrix M, from M* is [7]

$$M_{ij} = \left(\frac{\pm 1}{\det \mathbf{M}^*} \right) \cdot M_{ji}^* \tag{15}$$

The advantages of using reciprocal lattices in LEED pattern analysis becomes more evident when studying overlayer structures and patterns with domains. Detailed descriptions of these types of analyses are discussed in references [7,8].

So far only the positions of the diffraction beams have been considered. Analysis of the beam positions can be used to determine the geometry of the surface unit cell, but provides no information for the atomic positions within the unit cell, i.e. the basis. This information is contained in the diffraction beam intensities. The diffraction beam intensity as a function of electron energy is very sensitive to atomic positions, and thus provides a means of deducing the complete atomic geometry. There does not exist, however, a means of extracting a geometry directly from the IV curves. The most common approach is to employ a search technique, whereby calculated IV curves for a proposed theoretical model are compared to the experimentally obtained curves, then changes are made to the model until the two sets of IV curves are compatible. The techniques for structure searches are discussed further in Chapter 5. In the following section the basic elements for a kinematical theory of scattering are discussed, then some development is made toward describing a more complete dynamical theory.

Diffraction Intensities

The determination of the basis for a surface structure relies on the analysis of the diffraction intensities and their dependence on the incident electron energy. I present below a kinematical development, in which the effects of multiple scattering and inelastic scattering are ignored. Extensions to more complete dynamical theories which include these effects are then discussed. The

kinematical theory is accurate in predicting the general shape of IV curves, and provides a useful starting point for more complete dynamical theories.

The incident electron beam is represented by a plane wave, with wavelength λ, and direction given by unit vector $\mathbf{s}_0$, by

$$\psi = \psi_0 \cdot e^{i\mathbf{k}_0 \cdot \mathbf{r}} \tag{16}$$

where $\mathbf{k}_0 = (2\pi/\lambda)\mathbf{s}_0$ is the electron wave vector which also represents the crystal momentum of the electron. When the scattered wave is also represented as a plane wave, with wave vector $\mathbf{k} = (2\pi/\lambda)\mathbf{s}$, the scattered wave amplitude at position $\mathbf{r}$ due to scattering from atom j is [8]

$$\psi = \left(\psi_0 \cdot e^{-i\mathbf{k}\cdot\mathbf{r}}\right) \cdot f_j(\mathbf{k},\mathbf{k}_0) \cdot e^{i(\mathbf{k}-\mathbf{k}_0)\cdot\mathbf{R}_j} \tag{17}$$

The first term describes an outgoing wave, and f_j is the atomic scattering factor which depends in general on the initial and final wave vectors $\mathbf{k}_0$ and $\mathbf{k}$. The last term describes the phaseshift between the wave scattered from the j^{th} atom, at position $\mathbf{r}_j$, and a wave scattering from the origin. When all the atoms are considered, the amplitude must be summed,

$$\psi \propto e^{-i\mathbf{k}\cdot\mathbf{r}} \cdot \sum_j f_j(\mathbf{k},\mathbf{k}_0) \cdot e^{i(\mathbf{k}-\mathbf{k}_0)\cdot\mathbf{R}_j} \tag{18}$$

In the kinematical approximation, the sum over f_j is replaced by the so-called structure factor F [8], which depends on the geometry of the unit cell, the types of

atoms within the unit cell, and their respective positions, i.e. the basis. The vector $\mathbf{R}_j$, can be written in terms of the unit cell as

$$\mathbf{R}_j = n_1\mathbf{a}_1 + n_2\mathbf{a}_2 \tag{19}$$

which, along with F, can be substituted into equation (18) to yield

$$\psi \propto F \cdot e^{-i\mathbf{k}\cdot\mathbf{r}} \cdot \sum_{n_1}^{M_1} e^{in_1\mathbf{a}_1\cdot(\mathbf{k}-\mathbf{k}_0)} \cdot \sum_{n_2}^{M_2} e^{in_2\mathbf{a}_2\cdot(\mathbf{k}-\mathbf{k}_0)} \tag{20}$$

The upper limits of these two summations, M_1 and M_2, depend on the area of the crystal surface that the electron beam scatters from. The double summation is sometimes called the lattice factor G. The scattering intensity I, which is the physically measurable quantity, is thus

$$I \propto |F|^2 \cdot |G|^2 \tag{21}$$

The summations in equation (20) can readily be performed, giving

$$|G|^2 = \frac{\sin^2\left(\frac{1}{2}M_1\mathbf{a}_1\cdot(\mathbf{k}-\mathbf{k}_0)\right)}{\sin^2\left(\frac{1}{2}\mathbf{a}_1\cdot(\mathbf{k}-\mathbf{k}_0)\right)} \cdot \frac{\sin^2\left(\frac{1}{2}M_2\mathbf{a}_2\cdot(\mathbf{k}-\mathbf{k}_0)\right)}{\sin^2\left(\frac{1}{2}\mathbf{a}_2\cdot(\mathbf{k}-\mathbf{k}_0)\right)} \tag{22}$$

where M_1 and M_2 are the upper limits on the summations. This equation predicts directions $\mathbf{k}$ for the intensity maxima such that

$$\frac{1}{2}\mathbf{a}_1\cdot(\mathbf{k}-\mathbf{k}_0)=h_1\pi \quad \text{and}$$
$$\frac{1}{2}\mathbf{a}_2\cdot(\mathbf{k}-\mathbf{k}_0)=h_2\pi \tag{23}$$

where h_1 and h_2 are integers. An equivalent expression, using $\mathbf{k} = (2\pi/\lambda)\mathbf{s}$, is

$$\mathbf{a}_1\cdot(\mathbf{s}-\mathbf{s}_0)=h_1\lambda \quad \text{and}$$
$$\mathbf{a}_2\cdot(\mathbf{s}-\mathbf{s}_0)=h_2\lambda \tag{24}$$

These are the Laue conditions for diffraction from two dimensional lattices, which are equivalent to the Bragg equation, equation (8). The unit vectors $\mathbf{s}$ which satisfy these relations then determine the scattering angles for which the diffraction beams occur.

The intensity of a diffraction beam, at a given energy, depends on the first term in equation (21), namely the square of the structure factor, $|F|^2$. Recall that

$$F=\sum f_j(k,k_0) \tag{25}$$

where the f_j are the atomic scattering factors. The f_j can be expressed as a series expansion in angular variables [7,8],

$$f(\lambda,\varphi_G)=\sum_{l=0}^{\infty}(2l+1)P_l(\cos\varphi_G)e^{i\delta_l}\sin\delta_l \tag{26}$$

where φ_G is the angle between $\mathbf{k}$ and $\mathbf{k}_0$, and λ is $\hbar/k$. The P_l are Legendre polynomials, and the indices l are the same angular momentum quantum numbers that are used in describing the angular part of an electronic wave

function. The properties of scattering are contained in the phaseshifts δ_l, which are determined from the scattering potential used in the method described below.

The crystal scattering potential is generally approximated as a *muffin tin potential*, constructed from overlapping individual atomic potentials [9]. The muffin tins are spherically symmetric regions surrounding the ion-cores within the crystal, with radii defined by the distance for which the potentials for two adjacent ion-cores is equal. The regions between the muffin tin spheres are given a constant potential, which contains in part, the optical potential of the crystal. The optical potential consists of both a real and an imaginary part. The real part, called the inner potential V_0, is related to the index of refraction of the crystal, in that the electron experiences a change in kinetic energy inside the crystal relative to its energy in the vacuum. The primary effect of changes in V_0 is to shift the peaks in the IV data along the energy axis [7]. The imaginary part of the optical potential V_i characterizes the electron's energy loss through inelastic collisions, primarily with other electrons. It is directly related to the inelastic mean free path λ_{ee} for an electron in the crystal, by [8]

$$V_i = \frac{\sqrt{2mh^2(E + V_0)}}{\lambda_{ee}} \tag{27}$$

The optical potential cannot, in general, be derived from theoretical principles, but is determined empirically by choosing the set of V_0 and V_i which provide the best IV data.

Another important aspect of the scattering process is the exchange effect, due to the Fermi statistical behavior of the electrons. The effect of exchange is that electrons of the same spin states repel each other, and are attracted when their

spin states are different. This effect can be modelled by a potential, called the exchange potential. The exchange potential and the crystal potential characterize the scattering potential, which is the starting point for describing electron-solid scattering with the Hartree-Fock equation.

When written in the Born-Oppenheimer approximation, the Hartree-Fock equation can be written as [9]

$$\left[\left(-\hbar^2/2m\right)\nabla^2 + V_s(\mathbf{r}) - E\right]\cdot\varphi_o(\mathbf{r}) = -V_{ex}\cdot\varphi_o(\mathbf{r}) \tag{28}$$

where φ_o represents the incident electron wave function, and E is the electron energy. V_S is the crystal potential, and $V_{ex}\varphi_o$ is the exchange contribution to the interaction. The crystal potential V_S, from which the phaseshifts can be computed and the exchange potential V_{ex} are discussed below.

In the overlapping charge density model developed for the study of compound semiconductors [9,10], the potential V_α, for a particular ion core labelled by α, is expressed in terms of the electronic charge density $\rho_\alpha(r)$, the atomic number Z_α, and the ionicity I_α, as

$$V_\alpha(\mathbf{r}) = \frac{-Z_\alpha e^2}{|\mathbf{r}|} + e^2\int d^3r' \frac{\rho_\alpha(\mathbf{r}')}{|\mathbf{r}-\mathbf{r}'|} + \frac{I_\alpha M e^2}{d} \tag{29}$$

The last term in this expression contains the electrostatic Madelung sum M [11] for the crystal lattice, and d is the nearest neighbor distance. This term represents the electrostatic interaction of one ion core with all the others in the crystal. The effect is that the anion potentials are uniformly shifted negative by a small amount, and the cation potentials are shifted positive [10]. The integration

can be simplified by assuming that the charge density is spherically symmetric, i.e.

$$\rho_\alpha(\mathbf{r}) = \frac{\sigma_\alpha(r)}{4\pi r^2} \tag{30}$$

With this assumption, the expression for the potential near an ion-core is

$$V_\alpha(r) = \frac{-Z_\alpha e^2}{r} + \frac{e^2}{r}\int_0^r \sigma_\alpha(t)dt + e^2\int_r^\infty \frac{\sigma_\alpha(t)}{t}dt + \frac{I_\alpha M e^2}{d} + V_{ex}\{\rho_\alpha(r)\} \tag{31}$$

The last term is the exchange portion of the potential which is generally modelled by a functional of the charge density as will be seen below. This is the representation that is used to evaluate V_α numerically. The muffin tin crystal potential can then be constructed by superposing neighboring ion-core potentials.

The calculation of the phaseshifts from the potential is approached in a standard way [12]. The radial Schrodinger equation

$$\left(\frac{\hbar^2}{2m}\right)\frac{d^2R_l(r)}{dr^2} + \left[V_\alpha(r) + V_{ex}\{\rho(r)\} + \frac{l(l+1)\hbar^2}{2mr^2}\right]R_l(r) = (E + V_o)R_l(r) \tag{32}$$

is solved numerically out to the boundaries of the muffin tin spheres. The exchange potential in this equation is a functional of the charge density ρ. Also note that the inner potential, V_o enters into this expression. The logrithmic derivative of wave function $R_l(r)$ is matched to the solution outside the muffin tin, which consists of spherical Bessel functions j_l and n_l, at the muffin tin boundary [12].

The phaseshifts also depend explicitly on the exchange potential V_{ex}. The models for the exchange potential used in most LEED calculations are the Slater model [13] and the Hara model [14]. The contribution to the phaseshifts when using the Slater exchange model is [10]

$$\delta^{\text{Slater}}(E) \sim (1/k) \int_0^{r_{MT}} \rho^{1/3}(r) dr \tag{33}$$

and when using the Hara model, it is

$$\delta^{\text{Hara}}(E) \sim (1/k^3) \int_0^{r_{MT}} \rho(r) dr \tag{34}$$

These two expressions are valid in the limit that $k\, r_{MT} >> 1$. Note that the Slater effect falls off with increasing energy as 1/k, or $1/E^{1/2}$, while the Hara model decreases faster, as $1/E^{3/2}$. Because the Hara model is more sensitive to the charge density (it depends on ρ instead of $\rho^{1/3}$), the phaseshifts calculated with the Hara model are in general more sensitive to charge density variations. The Hara exchange model is used in this work because it has been shown to provide the best agreement between theory and experiment for compound semiconductors [10].

Once the phaseshifts, geometry, and the composition of the crystal have been specified, the diffraction intensities can be calculated. One popular method for compound semiconductors is called the T-matrix multiple scattering method [3,8,9]. This method utilizes a layer-by-layer approach in describing the scattering process. The calculations are performed in reciprocal space, where the scattering between layers and within the layers can be described with probability amplitudes

and matrix equations, which are more suitable for iterative calculations [3]. The details of this method are described in [3,8,9].

CHAPTER 3

EXPERIMENTAL TECHNIQUES

LEED

The experimental apparatus used in this work is depicted in Figure 7. The major components consist of the reverse view LEED optics, model RVL 10-120, from Princeton Research, an ultra-high vacuum chamber, a high resolution Pulnix model TM-840N CCD camera, and a Macintosh II personal computer. The sample is held by the vertical sample holder, which can be moved translationally in all three dimensions, and rotated about the vertical axis. The optics and electron gun are mounted on a formed bellows with adjusting screws for alignment normal to the sample surface. Heating to 500°C is possible by use of a button heater located at the sample base. A liquid nitrogen cold finger provides sample cooling capabilities to 150 K. The camera is interfaced to the computer through a Data Translation Quick Capture™ frame grabber board. The software package developed for this system, called *MacLEED*, is written in the MPW C programming language and utilizes standard Macintosh tool box functions and menu-type displays. Data acquisition for LEED with this arrangement is relatively easy, and a brief outline of the process is presented below. More detailed discussions of this system can be found in references [15] and [16].

The diffraction pattern is recorded by the camera and transferred to the computer as a standard composite video signal. The video signal is then digitized

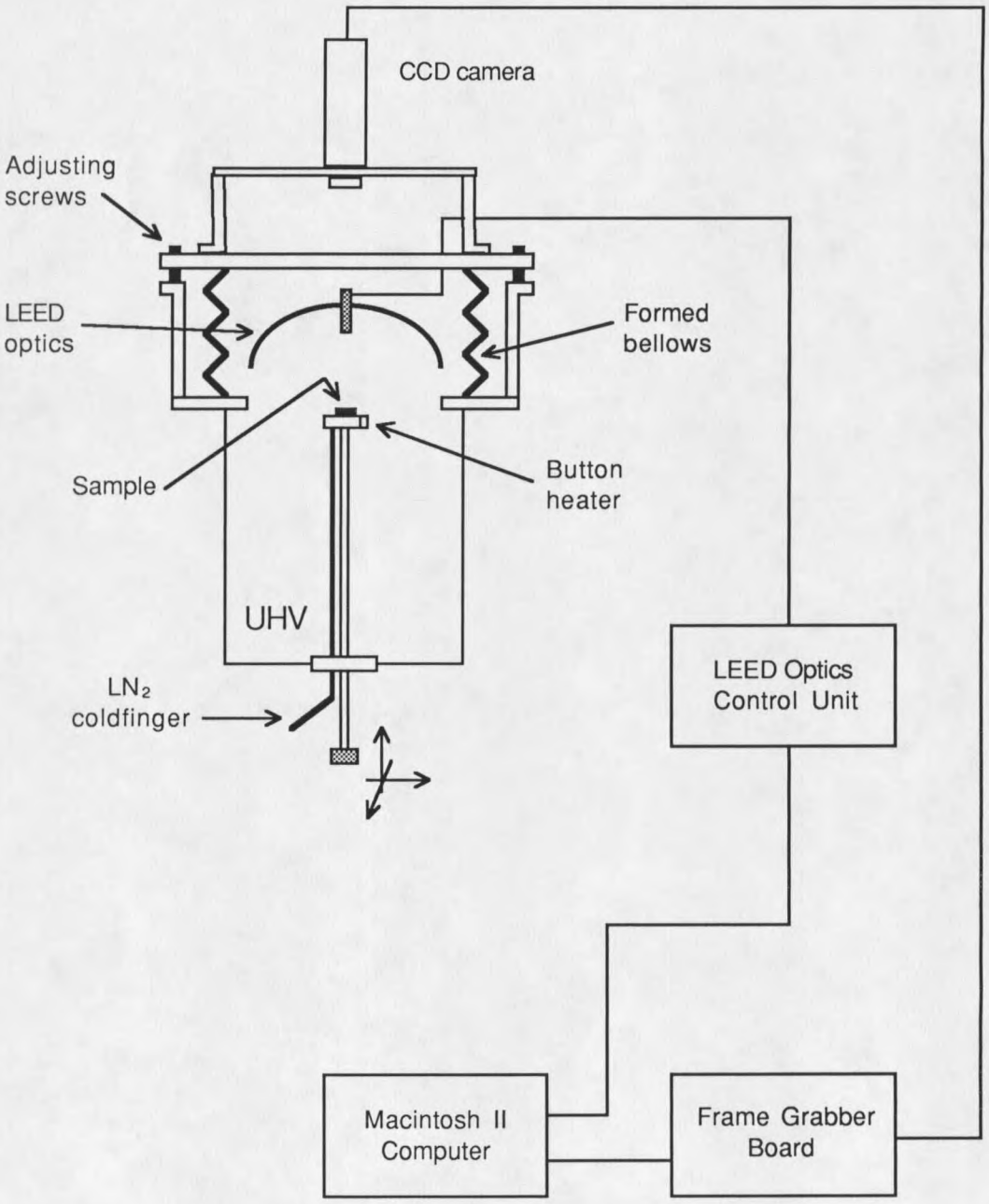

Figure 7: LEED equipment

by the frame grabber board one frame at a time, and temporarily stored in the board's RAM. The stored image can then be displayed on the computer monitor, or placed into the computer's memory for future analysis. A single frame, or video image is transferred from the camera to the computer every $1/30^{th}$ of a second. Thus, each frame corresponds to a light signal accumulated in a very short time. In order to get the best possible sensitivity with stored images, several (usually 16) frames are added together and stored as one single picture. An external timing circuit has recently been constructed which allows the video signal to be integrated inside the camera rather than through computer software techniques. A discussion of this circuit and its performance are given in Appendix B.

For the collection of IV data, the user must specify the incident electron energy range (typically 40-300 eV), the energy step interval (usually 2 eV), the diffraction beams of interest, and the number of frames over which each image is to be integrated. The specification of the diffraction beams is accomplished in three steps. First, an image is displayed for the LEED pattern at an electron energy near the beginning energy, then the positions of the diffraction spots are recorded. Next, an image is displayed for an energy near the top of the range, and the positions of the beams are again recorded. The user must then link the initial and final positions for each beam. The position of each diffraction beam is important because IV data is measured only for a small area surrounding each spot (usually 20x20 pixels).

From the two given positions and energy values, the computer calculates where the spots should be for each energy value in the specified range. The electron gun is then set to the starting energy, and the computer searches for an intensity maximum within a small rectangle centered on the expected spot

position. Once the maximum is found, the rectangle is centered on this maximum, the intensity is integrated, and a background subtraction is made by subtracting from the intensity the average value around the perimeter of the rectangle. The computer stores the intensity data, then advances the electron gun energy and the above steps are repeated.

For the collection of stored images, the user specifies the number of frames to accumulate and the electron gun energy. The computer then reads the frames successively from the frame grabber board, and stores the data in a 16 bit format, where the intensity values range from 0 to 255. The total accumulated signal is then divided by the number of frames. In this case, the entire image (619 x 422 pixels) is saved.

AES

The system can be readily converted to collect Auger data by changing a few electrical connections, as shown in Figure 8. This arrangement is known as the retarding field method. Several other methods for AES measurements have been developed, and are discussed in detail elsewhere [7,17]. The following discussion of the AES techniques used in this work is applicable to retarding field type AES systems in general.

A highly energetic (1-2 keV) beam of electrons is aimed at the sample, producing core-level excitations in the crystal atoms. De-excitation through the Auger process causes emission of outer shell electrons from the excited atoms. The kinetic energies of these electrons are characteristic of the electronic configurations of the emitting atoms, and thus provide a means of studying the electronic structure of the atoms in the crystal [17]. The AES technique is

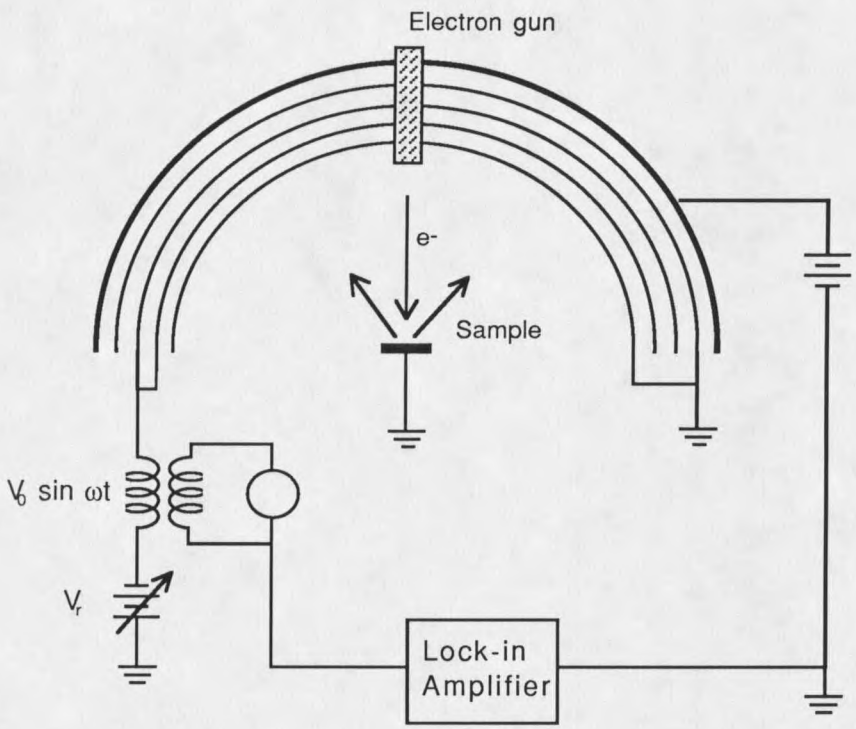

Figure 8: Electrical connections for AES

applicable to surface analysis because electrons emitted from deep within the bulk of the crystal lose kinetic energy to inelastic collisions before escaping to the vacuum. The effect of these electrons on the Auger spectrum is to increase the background intensity, leaving the main features of the spectrum to rely on atoms on or near the crystal surface. For most materials, the depth of AES sensitivity is about 10 atomic layers. When the Auger spectrum is analyzed, several properties of the crystal surface can be deduced, such as elemental composition and chemical bonding [17].

Referring again to Figure 8, the Auger electrons are filtered by grids 2 and 3 which are held at a potential V_r, known as the retarding potential. The

retarding potential provides a lower limit on the kinetic energy of the electrons allowed to pass through. When V_r is varied from $-V_{max}$ to zero, the current detected by the collector at a particular value of V_r is

$$i(V_r) = \int_{-eV_{max}}^{\infty} N(E)dE \tag{35}$$

where eV_{max} is the incident electron beam energy, and N(E) is the distribution of the electrons (number of electrons detected). This distribution appears as small steps on a large, slowly varying background [7,17]. A better resolution of the Auger peaks can be achieved by measuring the quantity dN/dE [17]. This quantity, however, is not directly measurable, but it can be measured indirectly in the following manner.

A small AC modulating voltage is superimposed on the retarding potential,

$$V_r' = V_r + V_0 \sin\omega t, \tag{36}$$

such that the collector current i, becomes a function of V_r', and the Taylor series expansion about $i(V_r)$ is

$$i(V_r + V_0 \sin\omega t) = i(V_r) + V_0 \sin\omega t\left(\frac{di(V_r)}{dV_r}\right) + \frac{V_0^2 \sin^2\omega t}{2!}\left(\frac{d^2 i(V_r)}{dV_r^2}\right) + \ldots \tag{37}$$

The terms in this expansion proportional to $\sin\omega t$ and $\cos 2\omega t$ are

$$A(\omega) = V_0\left(\frac{di(V_r)}{dV_r}\right) + \frac{V_0^2}{8}\left(\frac{d^3 i(V_r)}{dV_r^3}\right) + \ldots \tag{38}$$

$$B(2\omega)=\frac{V_0^2}{4}\left(\frac{d^2i(V_r)}{dV_r^2}\right)+\frac{V_0^4}{48}\left(\frac{d^4i(V_r)}{dV_r^4}\right)+\ldots \qquad (39)$$

The second harmonic component, $B(2\omega)$ of the collector current is then measured by a phase-sensitive (lock-in) amplifier. When V_0 is small enough, the first term in $B(2\omega)$ is dominant, and the measurement of $B(2\omega)$ is proportional to dN(E)/dE. The resolution with this system is ~8 eV for a modulation voltage of 8-10 volts. For most types of AES surface analysis, a much better resolution is necessary [17], but our resolution is adequate for the work presented here, in which AES was used primarily to monitor the relative changes in concentration of bismuth on the surface.

Data collection in the AES mode consisted of a few simple steps. The energy range was specified for each scan, along with a full scale sensitivity factor for the lock-in amplifier. The computer then controlled the retarding potential, and received the signal $B(2\omega)$, from the lock-in amplifier. Then the signal was converted to an x-y array and displayed on the computer monitor as a curve, dN/dE versus E. Once preliminary AES scans were made, it was only necessary to scan certain regions of the energy spectrum, corresponding to characteristic peaks for gallium, antimony, and bismuth. By comparing the changes in peak to peak ratios for the three elements, the relative changes in concentrations on the surface could be deduced.

Sample Preparation

Single crystal GaSb samples were single crystal bars with n-type doping, and carrier concentrations of ~1.7 x 10^{17} (cm^{-1}). Sample sizes were nominally 1.5" in length with .25" square cross sections. The orientation of the crystal was such that the (110) plane was perpendicular to the long axis of the crystal. A clean surface was obtained by cleaving the sample with a knife-edge along the (110) plane. To align the knife-edge parallel to the (110) plane, and thus minimizing steps and facets on the cleaved surface, small cuts were made in the sample with a diamond cutting wheel .045" deep, .020" wide, and spaced .080" apart. This is shown in Figure 9. The sample was then cleaned ultrasonically in a bath of acetone. Inside the chamber, the sample was held with the long axis vertical and cleaved with the horizontal knife-edge. The quality of the cleaved surface was immediately assessed by visual observation, and by observing the diffraction pattern as the sample was translated horizontally with respect to the electron beam. The surface was deemed acceptable, if a bright and clear p(1x1) pattern was observed.

To position the sample for an experiment, a region was searched for that gave a bright and consistent LEED pattern over a .020" x .020" area. The sample was then positioned so the electron beam struck the center of this area. Alignment of the electron beam perpendicular to the surface was achieved by turning the adjustment screws attached to the large bellows at the top of the chamber, see Figure 7. The alignment procedure was monitored by the computer, which displayed coordinates on the screen for both the actual and the desired locations of the primary reflection (00) beam. Adjustments were made until the positions coincided.

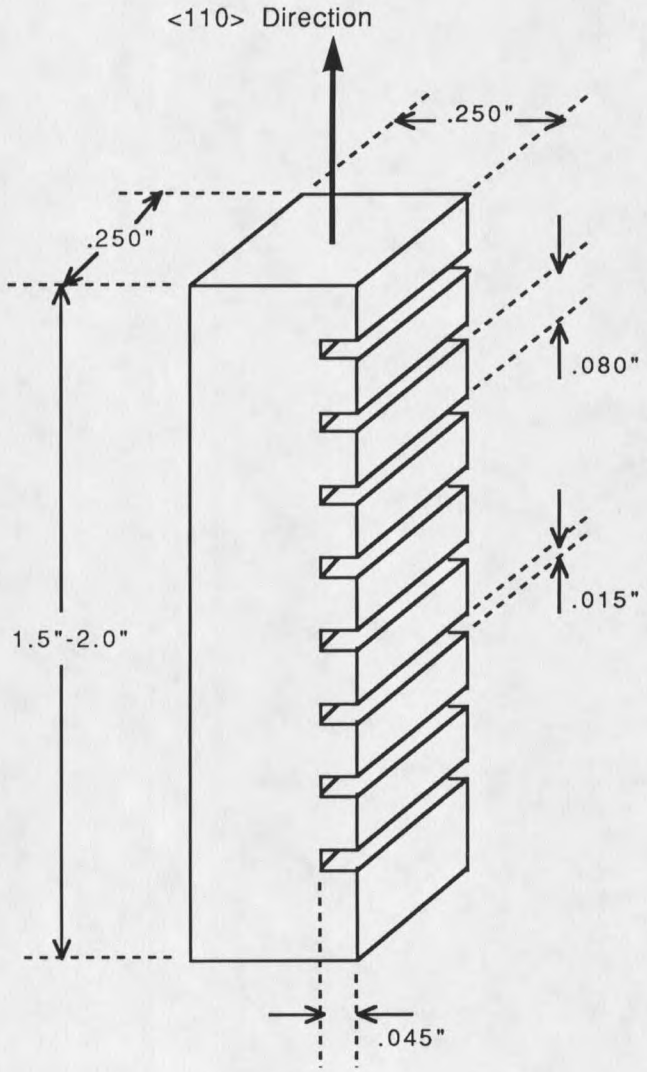

Figure 9: Sample preparation

QCO Calibration

The deposition of bismuth was achieved by evaporation from a solid piece of bismuth held in a tungsten basket. The crucible was heated to the sublimation temperature of bismuth (~600 °C), by placing the basket in a low-voltage high-current circuit. The deposition was monitored with a quartz crystal micro-balance oscillator held near the sample during evaporation. The change in frequency of the quartz crystal was calibrated to bismuth coverage on the sample in the following manner.

A quartz crystal has several modes of vibration, corresponding to several resonant frequencies. The most common mode used in micro balance applications is the shear mode along the AT-plane [18]. The resonant frequencies of the quartz crystals used in these applications is typically 4-5 MHz [18], and the frequency change for a coverage of a few monolayers is usually 10-100 Hz [19]. Over such a small frequency interval, the relationship between the frequency change Δf and the mass of the adsorbed material Δm is very nearly linear, and can be stated as [19]

$$\Delta f = C\,\Delta m \tag{40}$$

where C is a constant. This relation remains valid as long as Δf is much less than the resonant frequency (4-5 MHz).

For calibrating the micro-balance for an experiment, Δm is replaced by $\rho A \Delta\tau$, where ρ is the mass density of the adsorbed material, $\Delta\tau$ its thickness, and A is the area of the quartz crystal. Equation (40) then becomes

$$\Delta f = C\ A\ \rho\ \Delta\tau \tag{41}$$

Since the area of the crystal is also a constant, the equation can be written as

$$\Delta f = (1/k)\ \rho\ \Delta\tau \tag{42}$$

With the equation in this form, the constant k is referred to as the instrument sensitivity [19]. It is determined, in part, by the geometry of the micro-balance construction. For the micro-balance used in this work, the instrumental constant was determined to be 3.009×10^{-8} in cgs units. This was accomplished by comparing the frequency change as compared to that of a commercially-obtained oscillator. The accuracy of this method has been verified with Rutherford backscattering experiments, and the two methods agree to within about 10% [15].

In order to calibrate the QCO for bismuth adsorption on GaSb, the sticking coefficient for bismuth on the quartz crystal was assumed to be equal to that for GaSb. With this assumption, a change in the frequency of the oscillator is directly proportional to bismuth coverage on the sample. The goal of the calibration was to determine the amount of frequency change corresponding to a coverage of one monolayer, where a monolayer is defined as one bismuth atom per substrate atom on the GaSb(110) surface. In reference to equation (42), the product $\Delta\tau\ \rho$ is the surface mass density (g/cm^2) of the overlayer material, which was a convenient quantity to calculate first.

The (110) surface of a zincblende crystal has two atoms per surface unit cell, and a unit cell area of

$$A = \frac{a^2}{\sqrt{2}} \tag{43}$$

where a is the crystal lattice constant. For GaSb, a=6.095 Å, which gives a unit cell area of 26.27×10^{-16} cm^2. With two atoms per unit cell, the surface atomic density ρ_a is then

$$\rho_a = \frac{2}{A} = 7.61 \times 10^{14} \text{atoms} / \text{cm}^2 \tag{44}$$

The surface mass density was then found by multiplying ρ_a by the ratio of the mass number of bismuth divided by Avogadro's constant,

$$\Delta\tau \cdot \rho = \rho_a \cdot \left(\frac{209.0}{6.02 \times 10^{24}} \right) = 2.64 \times 10^{-8} \text{g} / \text{cm}^2 \tag{45}$$

Thus, the frequency change for one monolayer of bismuth on the GaSb(110) surface was determined to be

$$\Delta f = (2.64 \times 10^{-8}) \cdot \frac{1}{3.01 \times 10^{-8}} = 8.8 \text{Hz} \tag{46}$$

CHAPTER 4

GROWTH AND KINETICS OF Bi/GaSb(110)

Deposition and Growth of Bismuth

The first experiment was an attempt to reproduce the results obtained by Duke, *et.al.* [20] for the clean GaSb(110) surface. IV curves were measured at low temperature (150 K) for visual comparison with the previously-obtained data and to ensure that the clean surface characteristics were consistent with previous experiments. The IV curves matched very well, in that all of the major features of the curves were successfully reproduced. The symmetries of the clean surface yielded, as expected, a clear p(1x1) LEED pattern with a mirror reflection symmetry, (-h,k) = (h,k).

Next, a study of IV dependence on bismuth coverage was made. Both deposition and data collection were performed at room temperature. IV data were taken for several coverages, ranging from 0 to 2 monolayers, to determine whether long range symmetry existed in the bismuth overlayer. The results for the (0,1) beam are shown in Figure 10. The overall intensity gradually decreases with coverage, except for a slight increase near a coverage of about one monolayer, and the shape of the curve changes continuously up to about one monolayer. The changes incurred by the rest of the beams are similar to this, except for the (1,0) and (-1,0) beams (this effect is discussed below). Presented later in the discussion section is the conclusion that this continuous change in IV data together with the

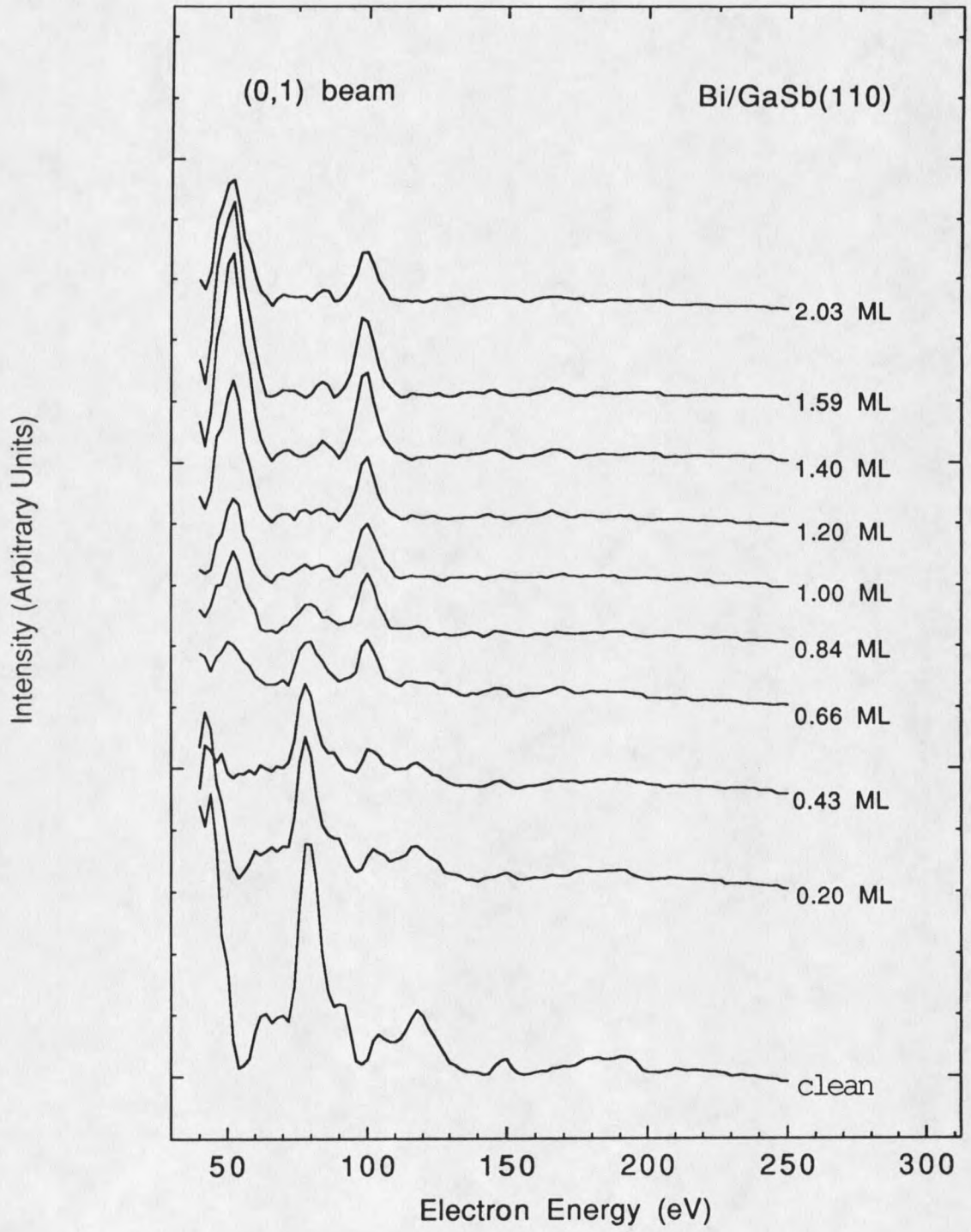

Figure 10: (0,1) diffraction beam dependence on bismuth coverage

increase in overall intensity of all but the (1,0) and (-1,0) beams is indicative of long range order in the one monolayer system.

The p(1x1) order and mirror reflection symmetry of the clean surface did not change with coverage. The retention of symmetry between the (2,1) and (-2,1) beams is shown in Figure 11. Since the intensities of the two beams are equal in magnitude, this also verifies the alignment of the electron beam perpendicular to the surface. Low temperature IV data was collected for the clean surface and at 1ML coverage for subsequent structure analyses.

Growth Kinetics and Annealing

The diffraction beam profiles were recorded at each of the coverages for different incident electron beam energies. For submonolayer coverages, an energy-dependent broadening effect on the diffraction beams was observed, but the effect was not seen for coverages of 1 ML or more. The effect was that some of the diffraction spots went from being sharp and well defined to diffuse and fuzzy,and then became sharp again as the incident electron energy was varied. A visual representation of this effect at a coverage of 0.4 ML is given in Figure 12. Figure 12(a) is a diffraction pattern image taken with an electron beam energy of 52 eV. Figures 12(b) and 12(c) correspond to 76 and 106 eV respectively. The effect can be seen for the (0,-1) and (1,0) beams. The location of the (0,-1) beam is at the lower right side of the images, and the (1,0) beam is located near the top of the images. The sizes of these two diffraction spots both increase from 12(a) to 12(b), and then decrease again in 12(c). The effect is visually more obvious for the (0,-1) beam. To further support this size effect, the spot intensity profiles for the (1,0) beam are plotted in Figure 13. The data for these plots were taken directly from the digitized images in Figure 13, and the profile maxima have normalized. Note that the

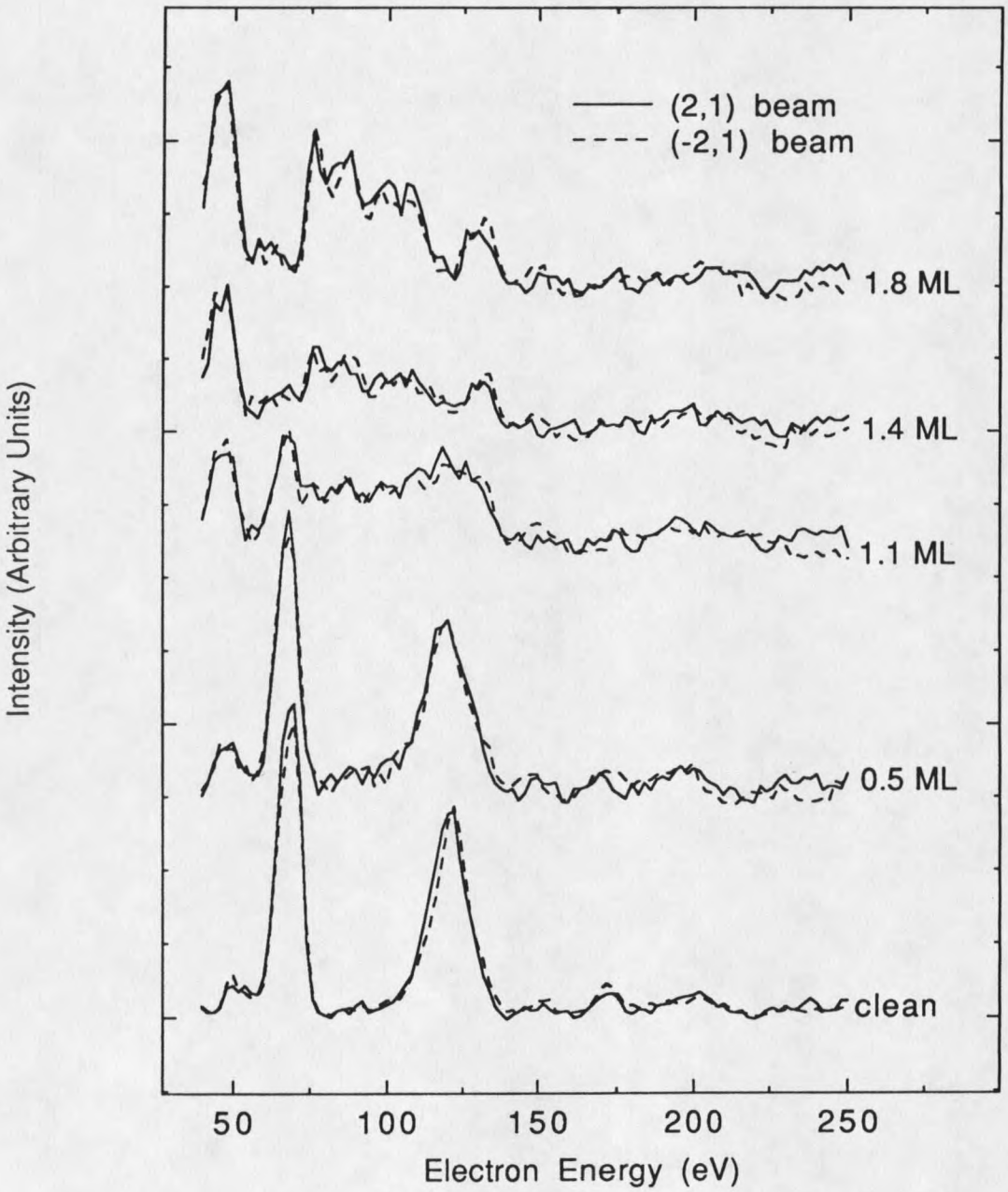

Figure 11: Symmetry retention between the (2,1) and (-2,1) beams

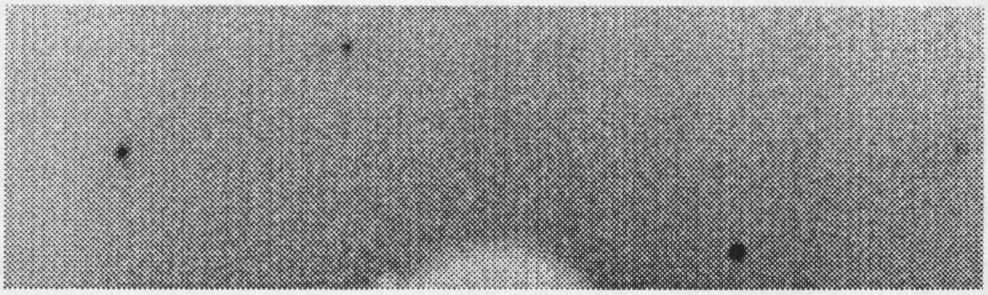

(a) 52 eV

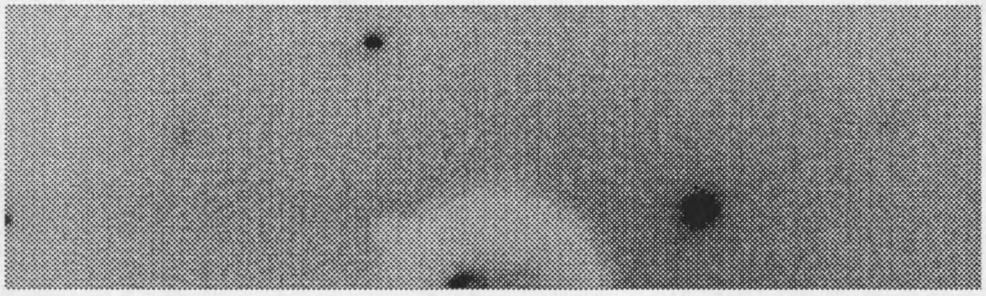

(b) 76 eV

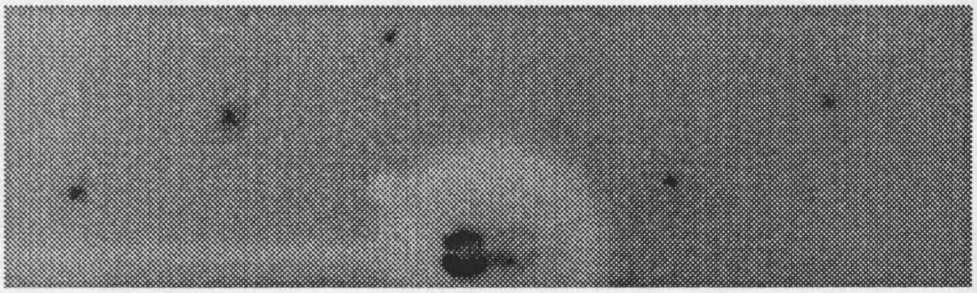

(c) 106 eV

Figure 12: Energy-dependent size effect

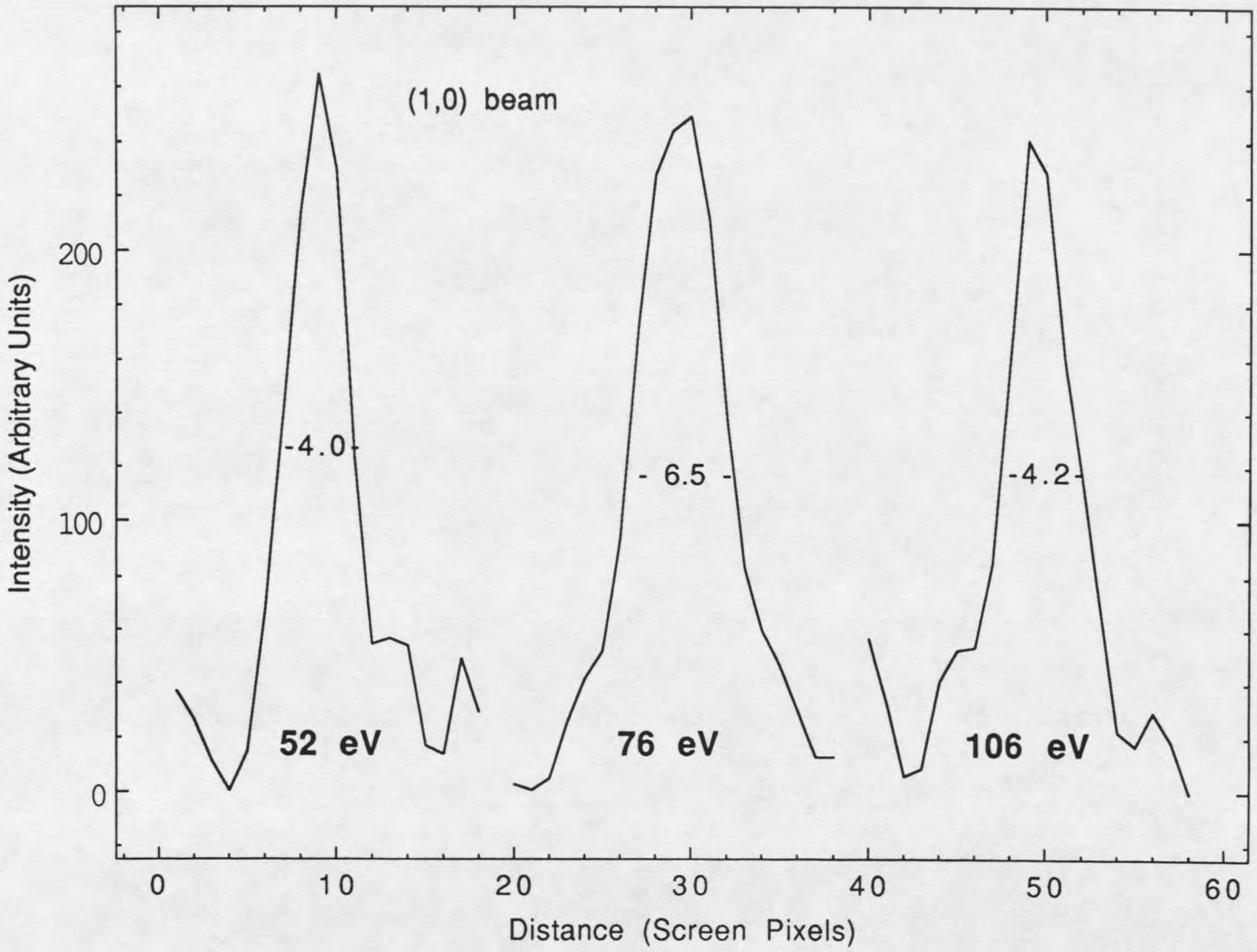

Figure 13: (1,0) beam profiles at different electron energies

changes in the full width at half-maximum (FWHM) of the profiles agree with Figure 12, in that the spot size increases, then decreases. An interpretation of this effect is given in the discussion section.

An important feature of the LEED pattern itself was that the (-1,0) and (1,0) beams vanished as the bismuth coverage approached one monolayer. The relative intensities for the (1, 0) and (0,1) beams are plotted in Figure 14. The intensity values used in this plot were obtained by integrating the IV curve over the energy range. As indicated earlier, the (0,1) beam experiences an increase in intensity near a coverage of about 1 ML, but the intensity of the (1,0) beam becomes very small at a coverage of about 1 ML, and remains small as more bismuth is deposited. It will be shown that this implies the surface structure for bismuth coverages above 1 ML is planar, causing destructive interference in these directions.

Annealing effects were then considered. The sample was given an initial coverage of bismuth and then subjected to a series of heating and cooling cycles. Several different annealing experiments were performed, with initial coverages ranging from 0.4 to 2.9 ML. In each case, the sample was annealed for about three minutes, at temperature intervals of 30-50°C, up to 350°C. Auger measurements were made initially and after every anneal cycle to establish the amount of desorption occurring at each step.

The most notable effect of annealing was a transition from the p(1X1) LEED pattern to a p(1x2) pattern, in which half-order spots formed along the k-axis of the LEED pattern. The transition began at an annealing temperature of about 100°C. For annealing temperatures above 350°C, the symmetry returned to p(1x1), suggesting complete desorption of the bismuth. For coverages of 1.5 ML or more, the transition became complete at an annealing temperature near 200°C. For

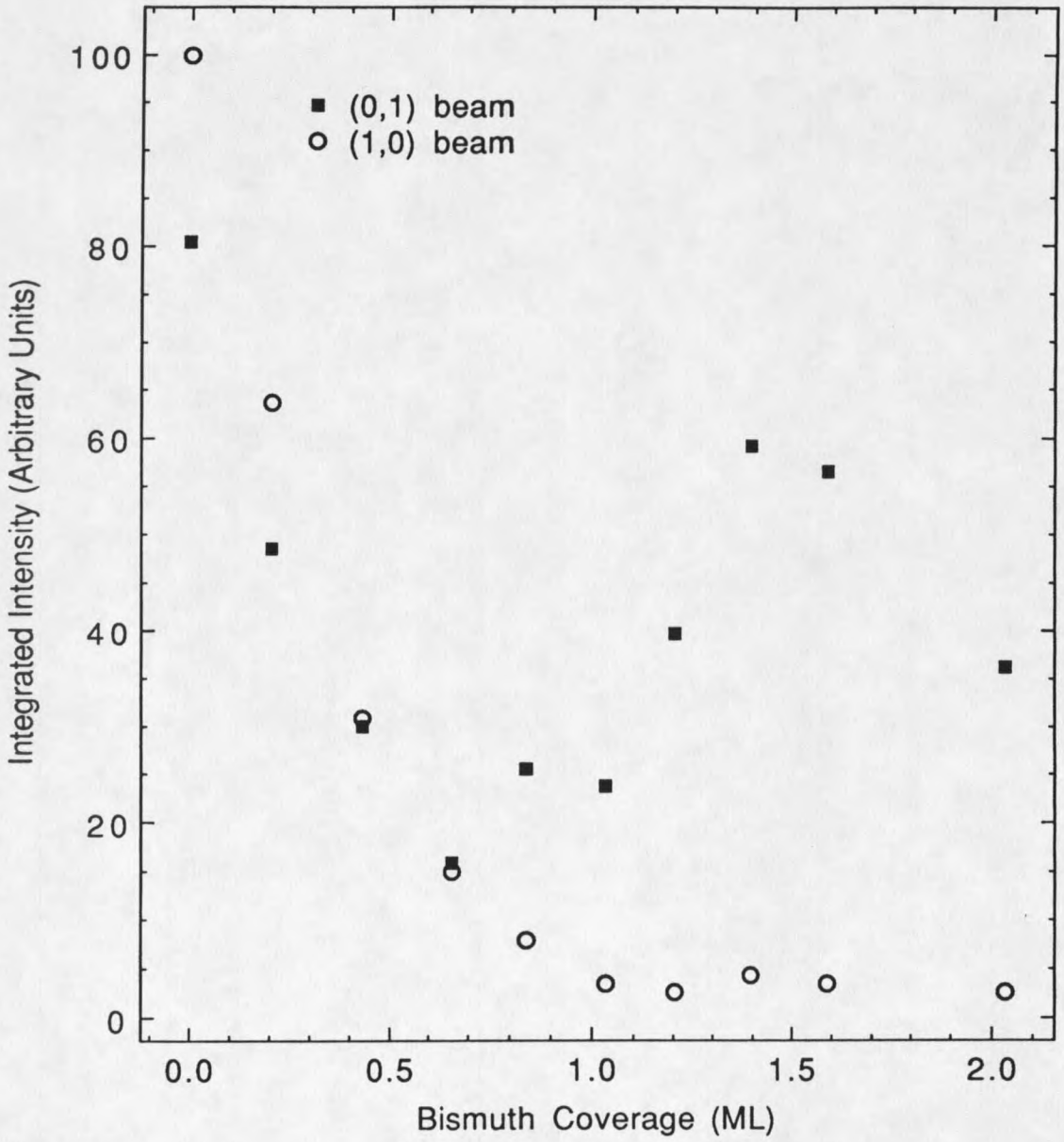

Figure 14: Relative intensities of the (0,1) and (1,0) beams at various bismuth coverages

submonolayer coverages, the transition was never quite completed, but faint streaks were seen to form between the diffraction spots along the k-axis of the LEED pattern. The transition to the p(1x2) symmetry is shown in Figure 15. The three pictures in this Figure correspond to digitized images taken with an initial bismuth coverage of 2.9 ML, and the electron beam energy for each of the images was 77 eV. The annealing temperatures are labelled for each of the images. The transition begins with streaks forming between the diffraction spots along the k-axis, as indicated in Figure 15(a). Figures 15(b) and 15(c) demonstrate that as the annealing temperature is increased, the streaks coalesce into well defined 1/2 order diffraction spots.

Shown in Figure 16 is a plot of the AES signals versus annealing temperature for the four initial coverages indicated earlier. The AES signal used was the peak to peak height of the 96-101 eV bismuth Auger feature. The portions of the plot corresponding to the p(1x1) and p(1x2) phases are labelled in the Figure. When the annealing process was begun with a coverage of more than 1.5 ML of bismuth, the transition to the p(1x2) symmetry was accompanied by bismuth desorption down 1.5 monolayer. For initial coverages less than 1.5 ML, no bismuth desorption was observed. This is also evident from Figure 16.

Discussion

The Ordered Growth of Bismuth

As indicated earlier, the growth of bismuth up to one monolayer appears to be an ordered process. One reason for this conclusion is that if the growth was purely disordered, or random, it would have contributed only incoherent scattering and hence no increase in the diffraction intensities would have been observed. Another reason is that the changes in the features of IV curves must

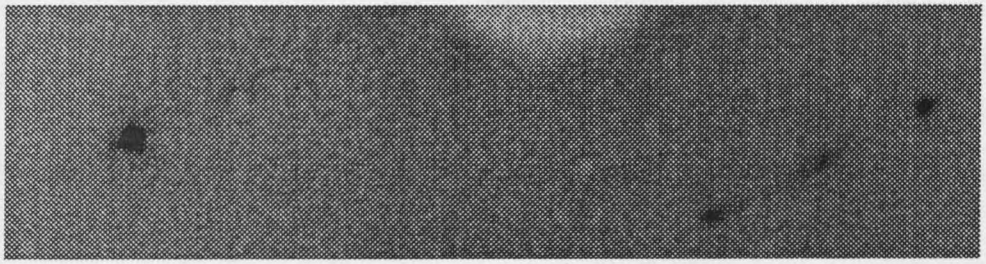

(a) 125°C

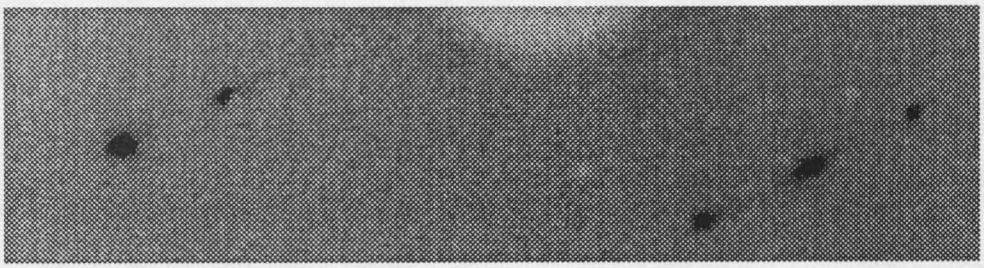

(b) 175°C

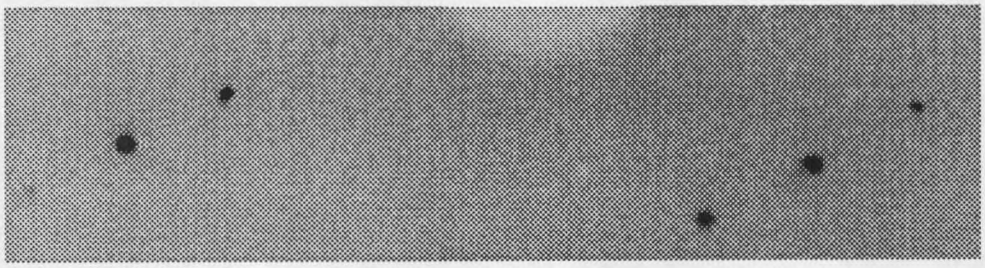

(c) 275°C

Figure 15: Formation of half-order diffraction spots

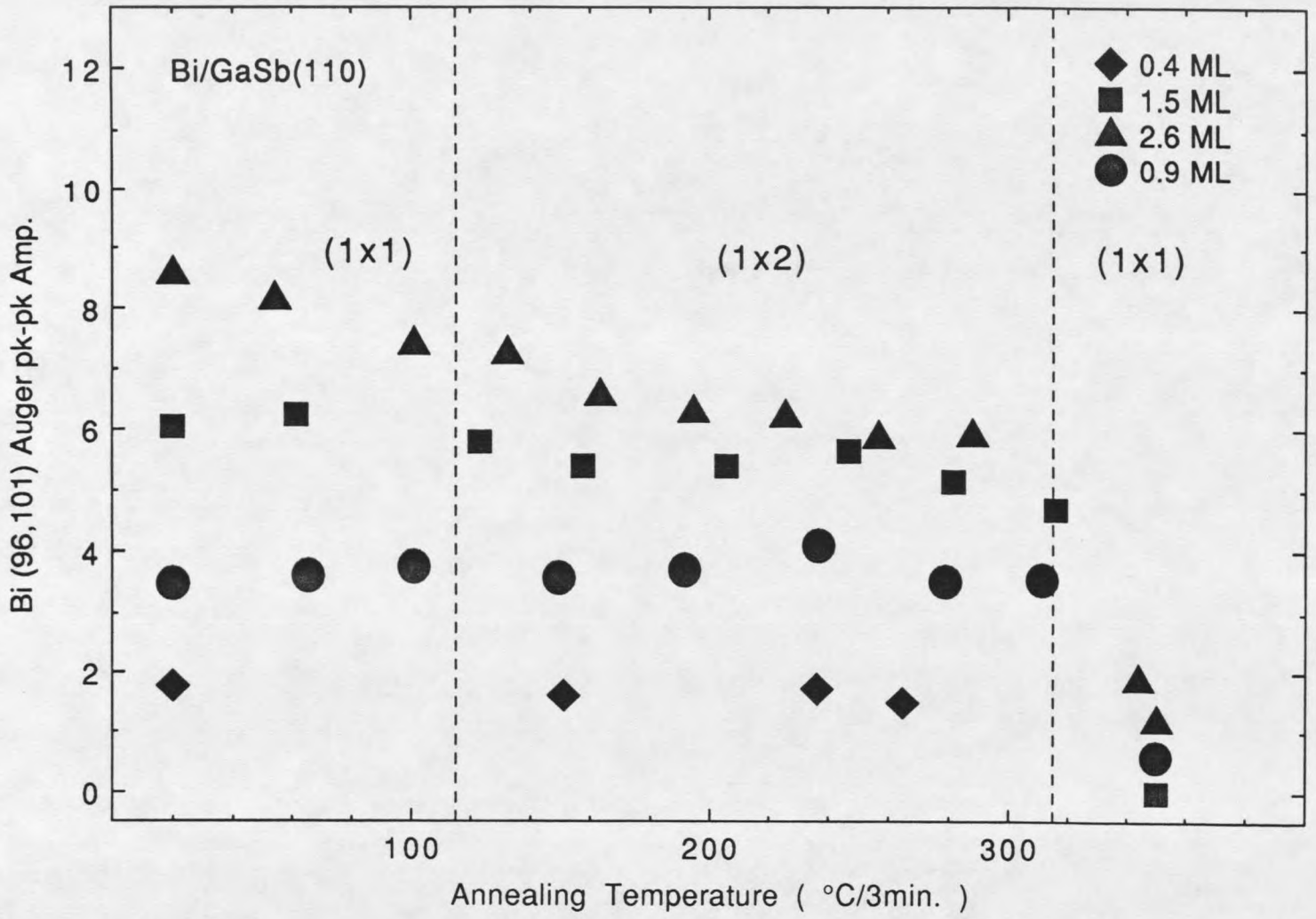

Figure 16: Bismuth Auger signal dependence on annealing temperature

have come from changes in the long-range order of the surface atomic geometry. These observations with growth of bismuth indicate that (1) long range order exists in the bismuth overlayer, or (2) the bismuth itself is not ordered but induces changes in the geometry of the substrate at the interface. The possibility that the changes in IV data are due solely to bismuth-induced reconstruction of the substrate, and not from long range order in the bismuth overlayer itself is discussed in Chapter 5. Since there are no additional changes in the features of the IV curves for higher coverages, the method of growth beyond one monolayer is no longer two-dimensionally ordered. This lack of order prevents further LEED analyses into the growth process above 1 ML.

The energy-dependent size effect discussed above further supports these conclusions. A similar size effect has also been observed with the Sb/GaAs(110) system [21], and more recently with the Bi/GaAs(110) system [4]. This effect has been demonstrated to be indicative of two dimensional ordered island growth of the adsorbate [22]. The absence of the effect at 1 ML and higher coverages indicates that the growth process beyond 1 ML is no longer via two-dimensional ordered islands. This is consistent with the changes observed in the IV curves, mentioned above.

A few comments can be made about the atomic structure of the 1 ML interface based on the observation that the (1,0) and (-1,0) beams became increasingly small for this coverage. If the surface were to have the truncated bulk structure of the (110) plane, these beams, as well as all (h,0) (h=odd) beams, should not have appreciable intensities due to an interference effect [3]. Since this effect was observed for the 1 ML coverage, it is suggested that the structure of the 1 ML bismuth overlayer system might resemble that of the truncated bulk structure.

This consideration was used in constructing a theoretical model for the 1ML atomic structure, which is discussed in Chapter 5.

The p(1x1) to p(1x2) Phase Transition

The phase transition observed upon annealing, in which the p(1x1) symmetry was replaced by a p(1x2) symmetry is now discussed. The k-axis of the LEED pattern, along which the periodicity changed, corresponds to the [001] direction on the crystal surface. The formation of half order LEED spots along this direction indicates the formation of a surface structure with long-range order, that has a periodicity of *twice* the unit cell of the substrate along the [001] direction. The gradual transition of the LEED pattern symmetry indicates a continuous change in the re-ordering of the surface atoms. Similar formations of superstructures have been observed with bismuth on other III-V(110) substrates [23].

CHAPTER 5

STRUCTURE ANALYSES

Program Overview

Searches were carried out for two different structures, that of the reconstructed clean surface, and the 1 ML p(1x1) bismuth overlayer. The parameters used in these two searches consisted of the bond lengths, bond rotation angles, and the real and imaginary parts of the optical potential. The justification for using these parameters will become evident in the discussion section of this Chapter, where it will be shown that the use of these parameters lead successfully to the determination of the reconstructed clean surface structure, which was in agreement with the results obtained by Duke, *et.al.* [20].

A general outline of the procedures used in the Bi/GaSb(110) structure searches is presented in Figure 17. The first step is the calculation of the atomic potentials. This was accomplished by a self consistent calculation, which started with the specification of an initial charge density. An atomic potential was constructed from the charge density, then the relativistic Hartree-Fock-Slater equation [9] was solved for the electron wave functions, using a local Slater exchange [13]. The wave functions were then used to calculate a new charge density, and the process was continued until convergence criteria were met, *i.e.* the potential and charge density were consistent with each other.

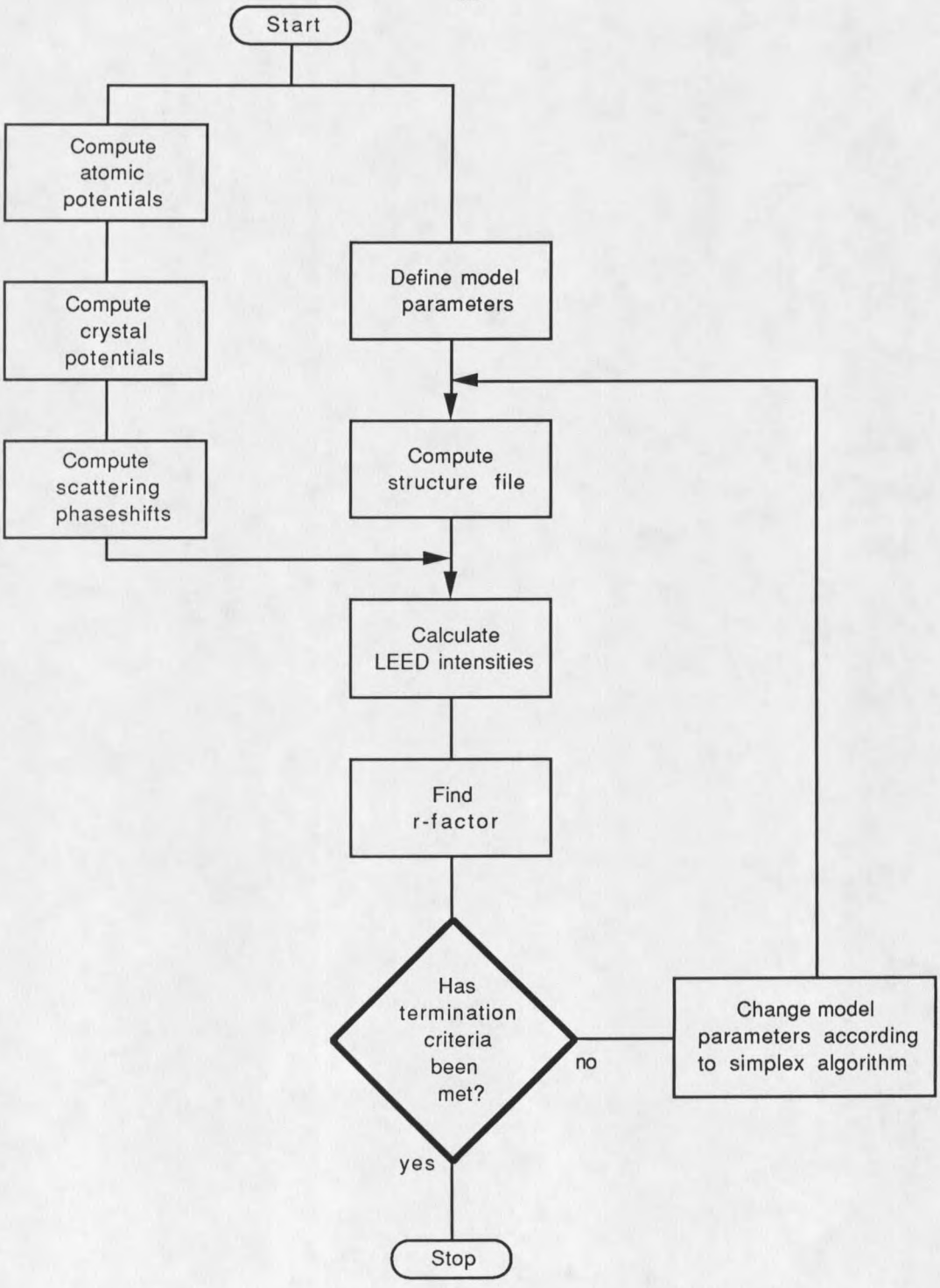

Figure 17: Flowchart diagram for structure search procedures

The crystal potential was then computed by overlapping atomic potentials in a manner described in Chapter 2. The atomic potentials and a crystal data file, which specifies the geometry of the crystal and its atomic composition were used as input for this step. For the 1 ML p(1x1) overlayer system, two separate crystal potentials were calculated, one for the overlayer, and one for the substrate.

The scattering phaseshifts were then obtained from the crystal potential, using the Hara model for the exchange potential. The phaseshifts were calculated for scattering from each atomic species in the crystal. For the clean surface only two sets of phaseshifts were needed, but if scattering from the bismuth overlayer was to be included, then three sets of phaseshifts were needed. The phaseshifts were calculated for l-values up to l=6, and are shown in Figure 18. The phaseshifts for higher angular momentum states were very small, and hence relatively insignificant in computing the scattering intensities. This is somewhat evident from Figure 18, where the phaseshifts for l=5 and l=6 remain close to zero over most of the energy range. Scattering cross-section versus incident energy plots were constructed from the phaseshifts in Figure 18, and are shown in Figure 19. The dashed lines in these plots represent the total scattering cross section, obtained from the individual cross sections shown with solid lines. These plots provide a more intuitive picture for the scattering dependence on incident energy. Most of the scattering is seen to occur for the energy interval 100-130 eV, for all three species.

The next step is to specify the initial model parameters, such as surface bond lengths, bond rotation angles, etc. The same phaseshifts were used throughout the search, even as the geometric parameters are varied, which introduced some error because the phaseshifts were calculated for a specific

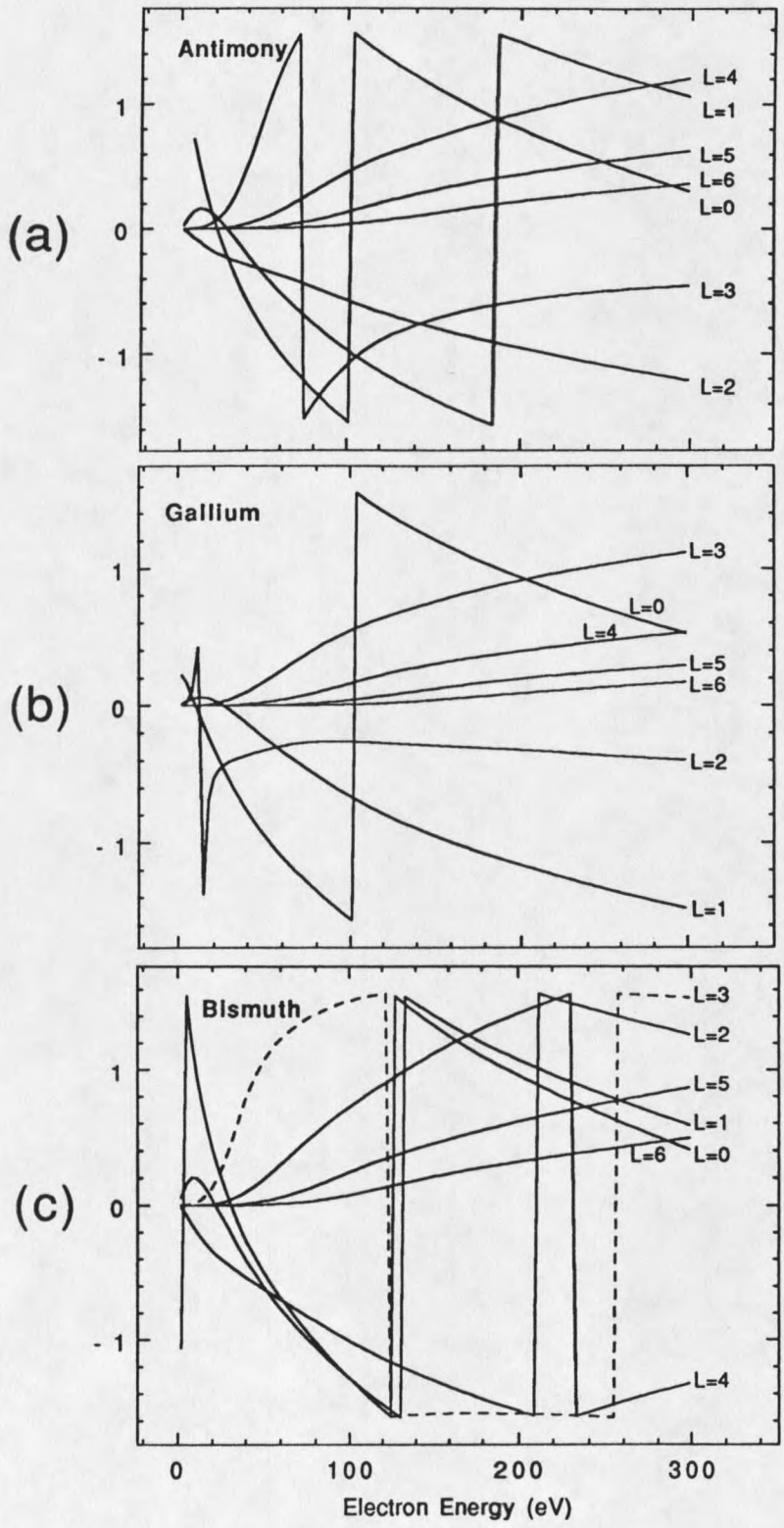

Figure 18: Scattering phaseshifts for (a) antimony, (b) gallium, and (c) bismuth

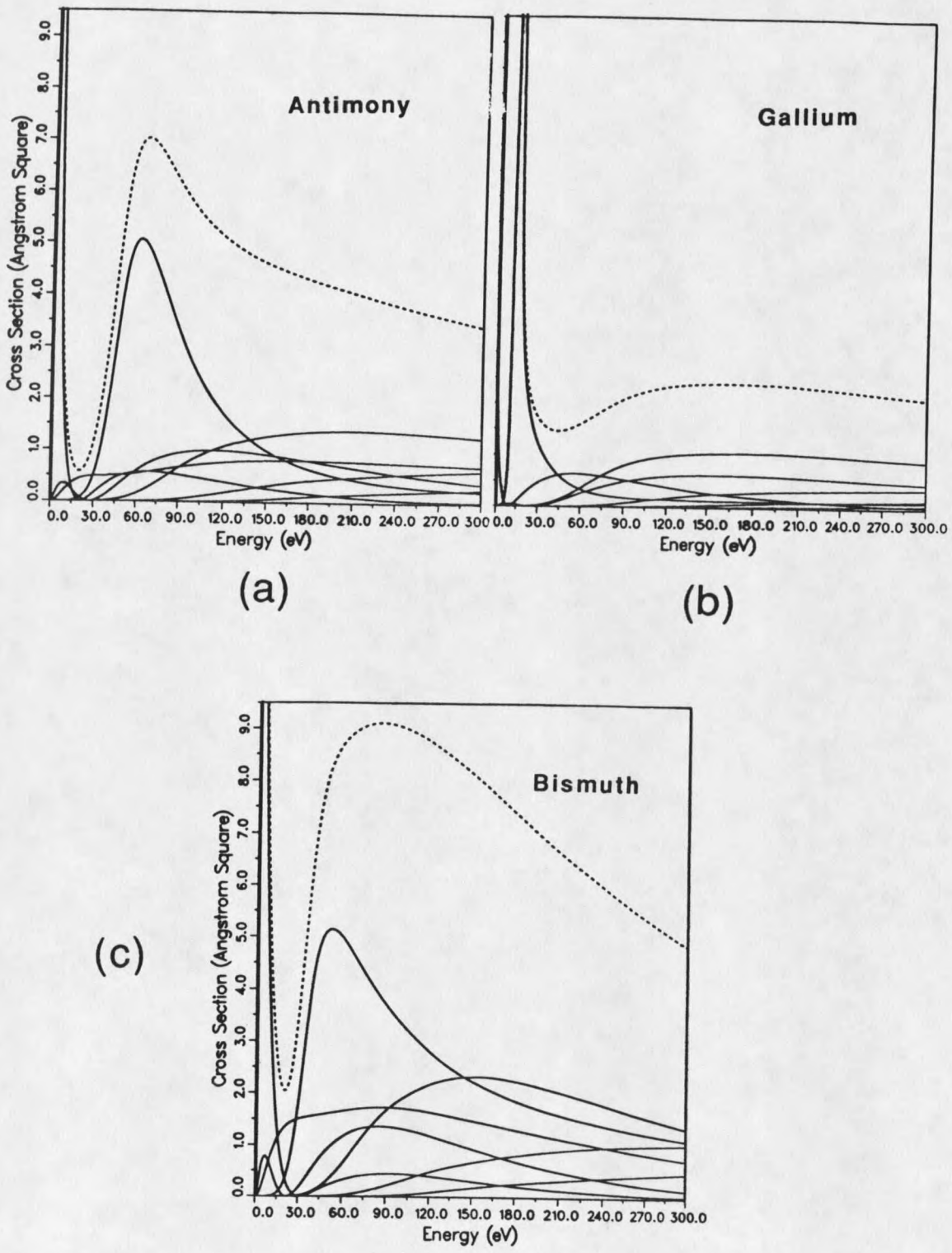

Figure 19: Scattering cross-sections for (a) anitmony, (b) gallium, and (c) bismuth

geometry. The error should have been small, however, and this method has been successfully utilized in work similar to that presented here [3,9]. The energy range and the diffraction beam indices were also specified at this stage. This information was then read into a *structure file*, which is a data file that specifies the model geometry, energy range, beam indices, inner potential, etc. of the model in a standard format, which can then be read by the main program *dynleed*, described next.

The structure file, together with the phaseshift files comprised the input for the main program, called *dynleed*. Dynleed was used to compute the LEED intensities for the directions defined by the Laue conditions, equation (24) at the energy values specified in the structure file. The program was written to utilize the T-matrix method mentioned in Chapter 2.

The resulting IV data was compared to the experimental data by the x-ray r-factor method [9], originally developed for use with x-ray diffraction studies. The r-factor method compares two sets of curves, x_e and y_e, such that

$$r_i = \frac{\sum_e (x_e - c_i y_e)^2}{\sum_e x_e^2} \tag{47}$$

where r_i is the r-factor for the i^{th} pair of IV curves, and the summation is performed over the discrete energy value index, e. c_i is a normalization constant defined by

$$c_i = \frac{\sum_e x_e y_e}{\sum_e y_e^2} \tag{48}$$

These summations are performed for each of the pairs of IV curves, and then an overall r-factor is determined from

$$R = \left(\frac{2}{3} + \frac{3}{2}\frac{1}{N}\right)\frac{\sum_{i=1}^{N} r_i \Delta e}{\sum_{i=1}^{N} \Delta e} \qquad (49)$$

In this equation, N is the number of pairs of IV curves, and Δe_i is the energy range for the i^{th} beam. This equation puts an emphasis on the size of the data sets being compared and is, essentially, taking the average of the individual r-factors r_i. The resulting r-factor R describes the degree to which the two sets of curves match. A lower r-factor means the proposed model provides a better fit to the experimental data.

The method of varying the parameters in searching for a best fit structure was based on the *simplex algorithm* (see Appendix A). With this method, the r-factor is used as the controlling factor in the search, and the simplex method converges on a model, i.e. the set of optimal parameters, with the minimum r-factor. The search was started several times for each proposed structure with different initial sets of parameters to ensure that a structure was found that gave the absolute minimum r-factor. Criteria for deciding how low an r-factor must be has been discussed by Duke [20]. In general, the LEED structure analyses are used in collaboration with other surface sensitive techniques, such as angle-resolved photoemission for confirmation of the results [3,7,8,9].

Discussion

GaSb(110) Clean Surface Geometry

Using the method described above, four different searches were initiated for the reconstructed clean surface structure, each starting with a different set of initial parameters. The diffraction intensities were computed for scattering from the first four layers of the model, and the scattering from the first three layers was computed exactly. Six phaseshifts were used for each atomic species. The results of these searches were in good agreement with the results previously obtained by Duke, *et.al.* [20]. The bond length parameters converged to values within 1% of the unreconstructed lengths, and the top layer rotation angle converged to 30° ± 1°, such that the top layer anion (antimony) was rotated away from the surface and the top layer cation (gallium) toward the surface. Shown in Figure 20, is a side view of the (110) surface with the bond lengths labelled as A, B, C, and the top layer rotation angle is labelled as ω_1. This bond length-conserving rotation is identical to that observed by Duke, *et.al.* [20]. When the values for the real and imaginary

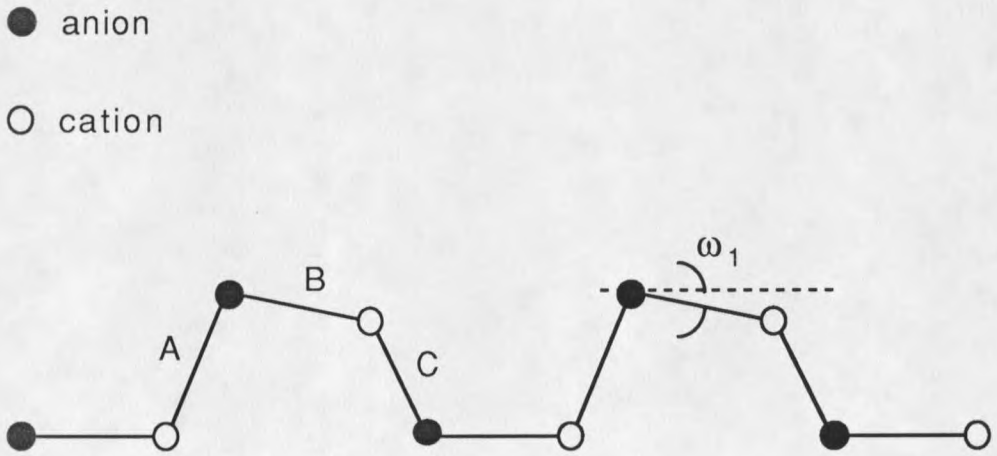

Figure 20: Side view of the III-V(110) surface, showing the bond lengths A, B, C, and the top layer rotation angle ω_1.

parts of the inner potential were also used as parameters, they converged to values of 10.1 eV for the real part and 4.5 eV for the imaginary part, which also agrees with previous results [20].

In each of the four searches, the r-factor values converged near 0.27, which is somewhat higher than what was previously obtained [20]. It took an average of 25 cycles for both the r-factors and the parameters themselves to converge to within 1%. Since a single cycle of the simplex loop required about one hour of computer CPU time, the clean surface structure search was not pursued any further. It will be shown in Appendix A that the simplex method converges quickly to the neighborhood of the final values, but the number of required cycles increases rapidly for a tighter convergence.

The set of IV curves for the converged structure are compared to the experimental curves in Figure 21. The experimental data are depicted with dashed lines and solid lines are used for the proposed model data. There are slight discrepancies between the data sets, but these results clearly indicate the validity of using the simplex method for LEED structure analyses. With this in mind, the same approach was used in analyzing the surface structure associated with the 1ML p(1x1) structure.

The 1 ML p(1x1) Structure

Analyses for two different 1ML p(1x1) model structures were attempted, which both failed to converge within good agreement with the experimental data. It thus appears that these two models are both incorrect for this particular structure, but the results of these calculations are still informative and important in that these two models can be ruled out. The first model which I call the disordered model, assumes no long range order in the bismuth overlayer. Instead

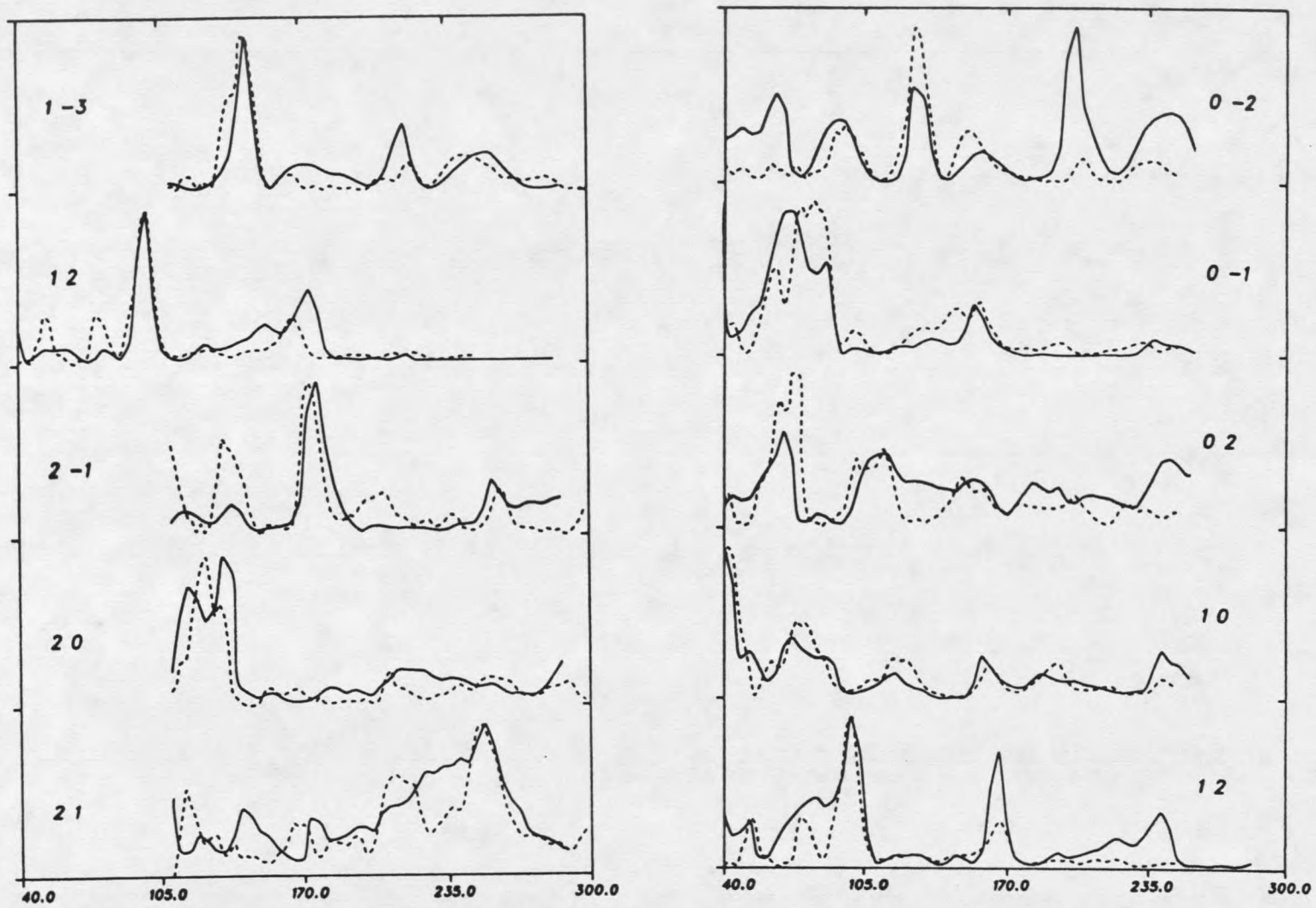

Figure 21: Comparison of calculated and experimental IV curves for the clean GaSb(110) surface. Dashed lines correspond to experimental data and the solid lines represent theoretical data.

it assumes that the changes in the IV data indicated in Figure 10 are due to bismuth-induced reconstruction of the GaSb substrate, with no contribution to the IV characteristics from the bismuth except for an overall decrease in intensity due to incoherent scattering. Hence, no bismuth phaseshifts were used in the analysis. As for the clean surface analysis, four different simplex-based searches were made. In each case the simplex search converged with an r-factor value between .43 and .46, and upon a different set of parameters each time. The converged geometric structures were widely different, as much as ±20° for the top layer bond rotation angle and 12% variation for the bond lengths. The convergence of the r-factor at such high values, together with the fact that an entirely different geometric structure was reached in each case suggests that the disordered model is inappropriate for this structure.

The second model used in the 1ML p(1x1) analysis was one in which the bismuth overlayer atoms occupy the vacant anion and cation sites at the surface, and the structure at the surface resembles that of the truncated bulk structure. The experimental results indicated that this was a favorable model, as mentioned in Chapter 4. This model is often called the Goddard model [25], and the 1 ML Sb/GaAs(110) system has been shown to have this structure [21]. Since the geometry of this arrangement is somewhat of an extension of the truncated bulk structure, the same geometric parameters were used as in the clean surface analysis, see Figure 20. The bonding configuration of this arrangement is discussed by Skeath *et.al* [25]. Again, four different searches were made. The results were similar to those obtained for the disordered model, in that the r-factor values converged at high values (.41-.50), and the converged geometric parameters corresponded quite different structures in each case. An average of 24 cycles were completed in the simplex loop for the search using this model. These results

indicate, as with the disordered model, that this model is inappropriate for describing the 1 ML p(1x1) structure, which consequently must be quite different from the truncated bulk structure.

CHAPTER 6

SUMMARY AND CONCLUSIONS

From the results of the experimental observations presented in Chapter 4, the power and utility of surface analysis with LEED has become evident. Several conclusions about the qualitative characteristics of the growth and kinetics of bismuth on GaSb(110) were reached. Currently, developments are being made toward more quantitative approaches to the analysis of the experimental data. For example, a collaborative effort is currently in progress with members of the MSU chemistry department for a more rigorous and systematic analysis of the diffraction spot profiles, which will lead to a better understanding of the kinetics involved in the growth and annealing processes.

The results of the clean surface calculations indicated that the simplex algorithm is quite adequate for minimizing the r-factor and finding the correct model parameters. This further supports the conclusion in Appendix A, that the simplex algorithm can be successfully used in the determination of atomic structures with LEED calculations.

The effort to determine the structures of the bismuth overlayer systems is being continued and developed further at this time. Currently, work is being done in developing other models for the 1 ML p(1x1) structure, based on the considerations of the experimental observations for this and similar systems, and on the results of similar structure searches [26].

APPENDICES

APPENDIX A

SIMPLEX ALGORITHM

The simplex algorithm, first proposed by Nelder and Meade in 1965 [27], is a minimization routine for multivariate functions based on geometric principles. Advantages of using this algorithm are that it does not require numerical calculus or matrix manipulations, and that it makes no use of one dimensional minimization techniques. One disadvantage is that it is not very efficient in the number of function evaluations that it requires. A description of the algorithm, and how it was incorporated into the structure search process is presented below.

A simplex is defined as the geometrical figure consisting, in N dimensions, of N+1 vertices. Connecting lines and polygonal faces are considered part of the simplex. In two dimensions, a simplex is a triangle, and in three dimensions it is a tetrahedron. A necessary restriction on the simplex is that it be non-degenerate, i.e. it must contain a finite volume of dimension N. Without this requirement, the simplex would be confined to a space of dimension less than N, and the function parameters would be similarly constrained.

For the minimization of function of N parameters, an initial simplex is constructed by arbitrarily choosing N+1 sets of function parameters. These sets of parameters then define the initial vertices. The response of the function is found for each of the vertices, and a search is begun for a parameter set which gives the lowest function value. This is achieved by "moving" the simplex through the space defined by the function parameters, through a series of *operations* and

decisions which exchange old vertices for new ones that give better, i.e. lower, function response values.

The first steps in "moving" the simplex are to determine the best, worst, and second worst vertices, and then to find the centroid of the hyperplane defined by all the vertices except the worst. Then one of 4 operations is performed, as shown in Figure 22 for the two dimensional case. The boldface triangles in the Figure represent the initial simplexes, and the new vertices found by each of the operations are labelled accordingly. Associated with each operation is a coefficient α, which represents the length ratio defined in the Figure. These coefficients are decided upon before the minimization routine is started. The choice of values for these coefficients is arbitrary, and usually based on intuition and experience. The values used in the program described in Chapter 5 are: $\alpha_r=1$, $\alpha_e=2$, and $\alpha_c=\alpha_s=1/2$.

The simplex decision-making algorithm is depicted in a flowchart format in Figure 23. Here, a procedural outline is given for deciding where to look for new vertices, and when to exchange old vertices for new ones. In this Figure, nworst represents the second worst vertex. Note that the vertex found by the reflection operation is not kept unless the function response is better than the *second* worst value. This is because the newly acquired vertex would then be the worst vertex, and the next operation would be a reflection back to the previous worst vertex, requiring a repetitious function evaluation. Examples of computer programs utilizing the simplex algorithm can be found in references [28] and [29].

The simplex algorithm was incorporated into the Bi/GaSb(110) structure searches by using model parameters such as bond lengths, bond rotation angles,

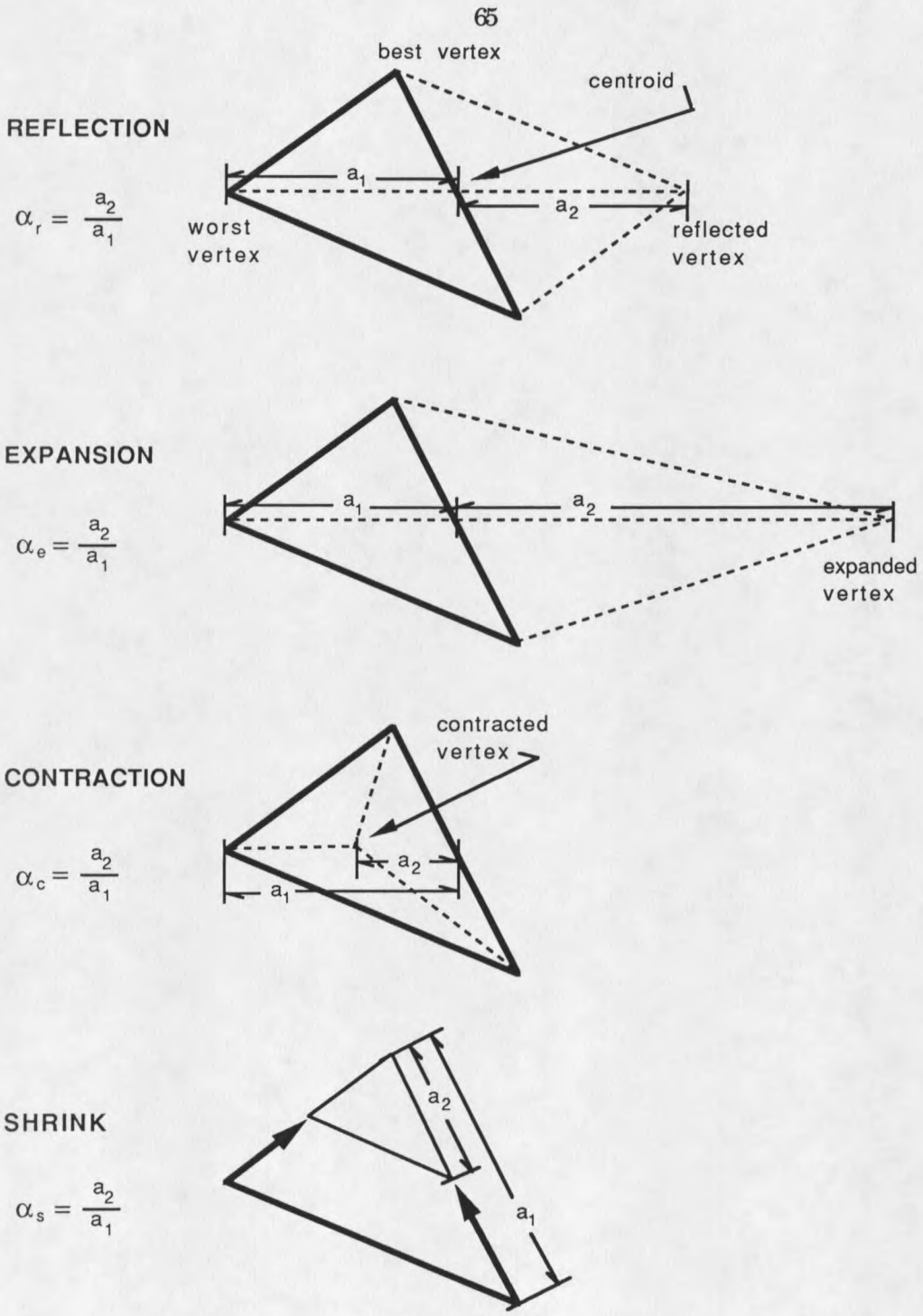

Figure 22: Simplex operations in two dimensions

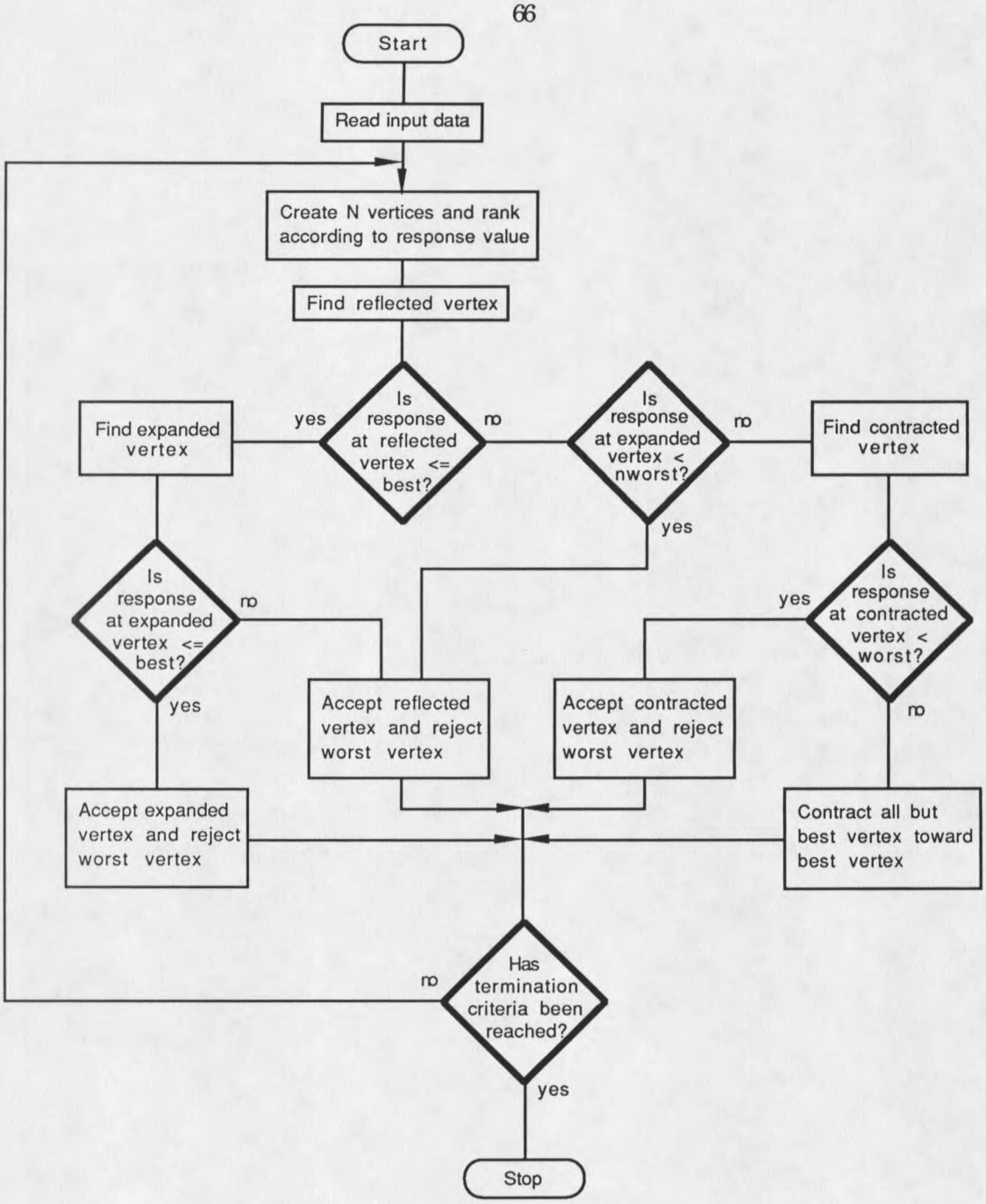

Figure 23: Flowchart for the Simplex Algorithm

and the inner potential as the function parameters, and letting the r-factor for a given model calculation represent the function response. The applicability of this approach was tested with a trial structure for several different starting simplexes, for both correct and incorrect structural models. The experimental data used in these tests were the clean GaSb(110) IV data, for which the correct atomic structure has been determined [20].

The convergence of the r-factor, for these tests is shown in Figure 24(a). The results for six different searches are shown here, with the solid lines corresponding to the correct model, and the dashed lines representing the use of an incorrect model. When the correct model was used in the search, the r-factors converged very near to the same value all three times, but the use of an incorrect model caused the r-factors to converge to quite different values for each search. For the searches made with the correct model, about 20-30 cycles were required for the r-factor to converge to within a comparatively small deviation from the final value. Additional convergence of the r-factor values required many more cycles, which is evident from the Figure.

A comparison of the r-factor convergence to the convergence of the model parameters for one search is shown in Figure 24(b). The dashed line represents the percent standard deviation of the r-factor value, and the solid lines correspond to the model parameters. For this particular search, the parameters converged at approximately the same rate as the r-factor. This is representative of all of the test searches, even when the incorrect model was used. In this Figure, a reasonable convergence was reached after about 30 cycles of the simplex loop, and additional convergence was comparatively slow. The other test searches converged similarly after 20-30 cycles.

The results of these test searches indicate that the simplex-based search converges quickly up to 20-30 cycles, and much slower thereafter. They also indicate that when the correct model was used in the search, the simplex search converged toward the same structure each time, and that the use of an incorrect model led to different structures each time. Based on these results, the simplex-based search method appears to have merit for use in LEED structure analyses, in that a discrimination can be made between correct and incorrect structural models.

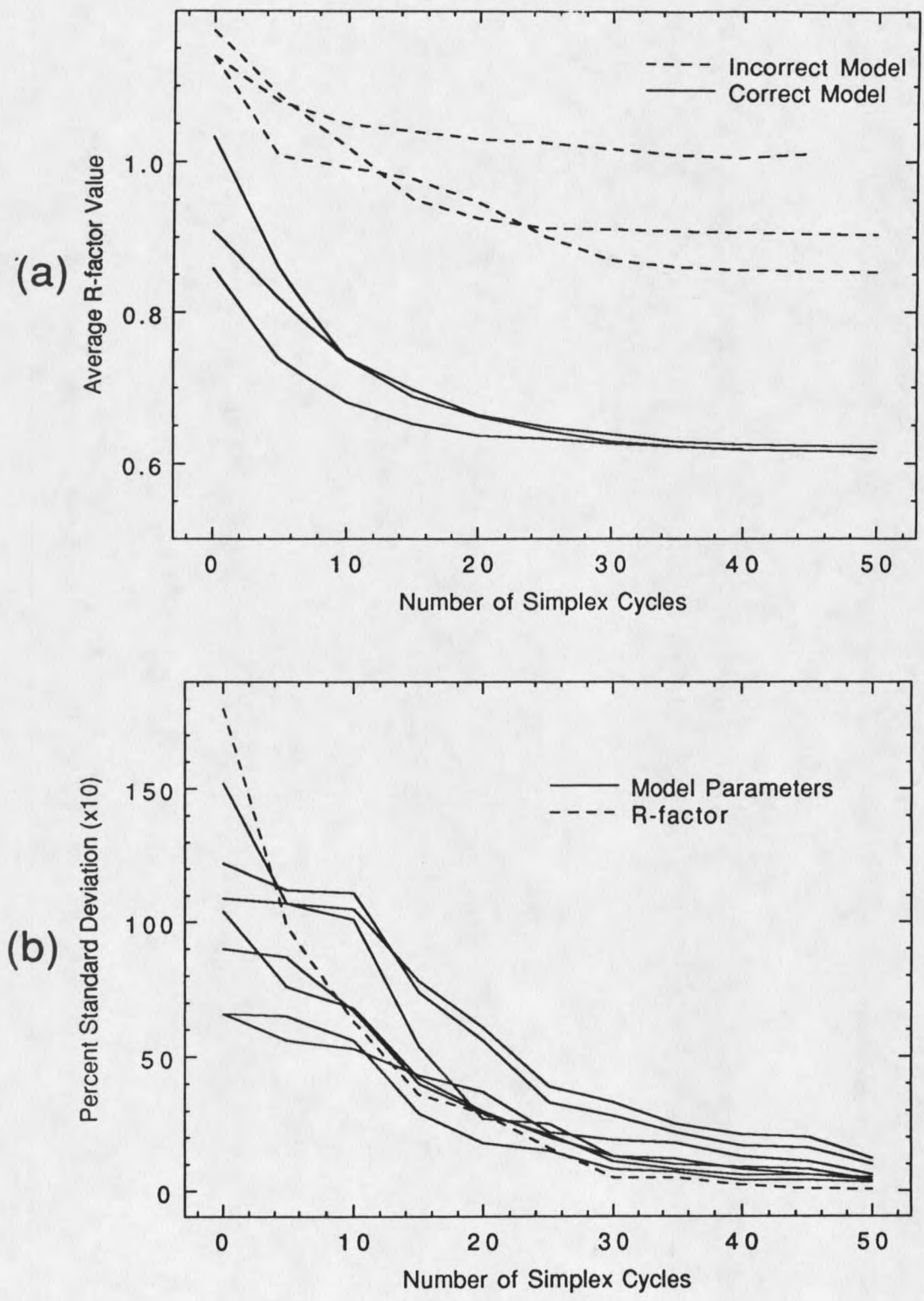

Figure 24: Results of simplex convergence tests, (a) Average r-factor values, (b) Convergence of model parameters compared to r-factor convergence.

APPENDIX B

VIDEO CAMERA TIMING CIRCUIT

I present in this section a discussion of the timing circuit designed to facilitate using the video camera in the random-integration mode, but first some fundamental features of the video signal itself are presented.

The output signal from the video camera follows the standard interlaced video format where one frame, or complete image, is composed of an odd and an even field. The fields correspond to the horizontal lines of the video signal. The odd field contains the video signal for the odd-numbered lines and the even field contains the even-numbered lines. The two fields together form the interlaced frame. Figure 25(a) shows the camera output when used in the normal operating mode. It is composed of alternating odd and even fields, each separated by a vertical sync. The vertical syncs occur with a frequency of 60 Hz so a complete frame is transferred every $1/30^{th}$ of a second. As seen in the Figure, the video output utilizes a 1V peak-to-peak timing signal. Within the camera a single CCD array is used to measure the light signal for both fields. In the normal operating mode, the CCD array reads the light signal for $1/60^{th}$ second for each field, transfers the field signal, then reads the signal for the next field, and so on. This particular camera (Pulnix Model TM-840N) is equipped for random-integration output, in which the CCD array can be instructed to read the light signal for any desired length of time (longer than $1/60^{th}$ sec). This feature is useful in low-light

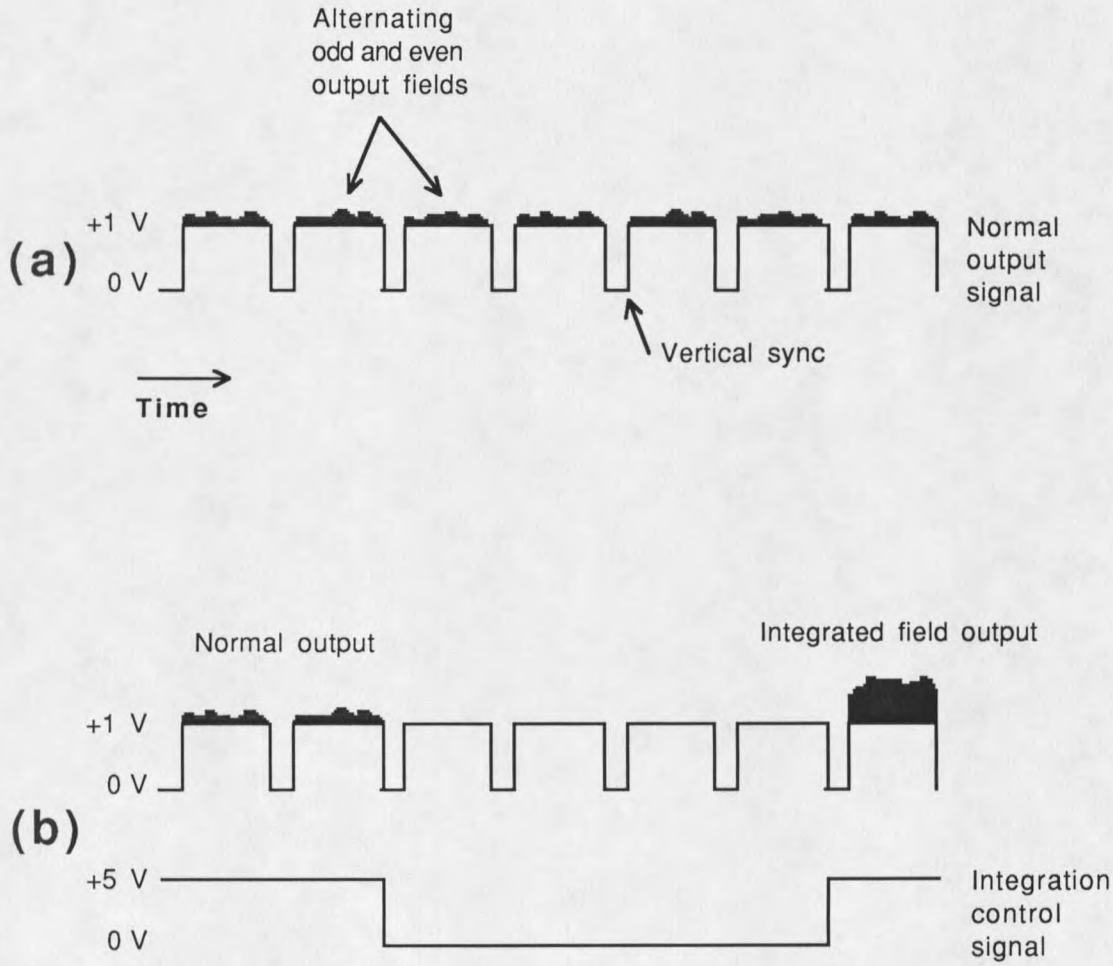

Figure 25: Video camera output signals

applications, where an accumulated, *i.e. integrated* signal is necessary for adequate sensitivity.

In order to use the integration control feature, an external TTL or CMOS binary signal must be supplied to a pin connection on the back of the camera. When this signal is held *low* (0 Volts), the output from the CCD array is inhibited. When the signal is switched to *high* (+5 Volts), output begins at the next vertical sync. This is shown in Figure 25(b). Note that the camera output always contains the basic timing signal, and only the superposed light signal is affected by using the integration control. Also note that when using the integration control, only one field can be integrated at a time, and the integrated fields are separated by the time of integration. The importance of these features will become obvious in discussing how the timing circuit was constructed.

The Quick Capture™ frame grabber board which is used to digitize the video signal is designed to read one complete frame, or two consecutive fields, at a time. But when the camera is used in the integrating mode, the integrated fields do not appear consecutively. Rather than trying to separate and recombine the integrated output signal, an alternate approach was used which is described below.

The digitizing board has the provision for an *external trigger*, to initiate digitization. Use of the external trigger requires a TTL signal also. Digitization then begins after the vertical sync which follows a low to high transition of the external trigger connection. So when the external trigger is properly used, digitization can be initiated for each of the frames containing the integrated fields. Each of these frames contains only one integrated field, so when they are digitized and read into memory, they must be added together to make a complete integrated image. Presented next is the TTL circuit developed for these applications.

A schematic description of the circuit is presented in Figure 26. The base timing signal from the camera is used to provide the initial signal. The 1V signal is adequate for use in TTL circuits. This signal is passed through a series of timing circuits, which change the timing of the signal to allow for integration times corresponding to an integral number of frames, *i.e.* multiples of $1/30^{th}$ of a second. The design of the circuit allows for integration times of 33, 66, 99, 233, and 363 microseconds. The camera output resulting from the use of this timing circuit is shown in Figure 27. Also shown in Figure 27 is the signal to be used for the external trigger, which is the same as the integration control signal. The timing of this signal is such that only the frames containing the integrated fields are digitized.

This timing circuit represents the first step toward using the video camera in the integrating mode. Complete incorporation of this circuit will require further refinements in the data acquisition software so the integrated frames can be combined and stored correctly.

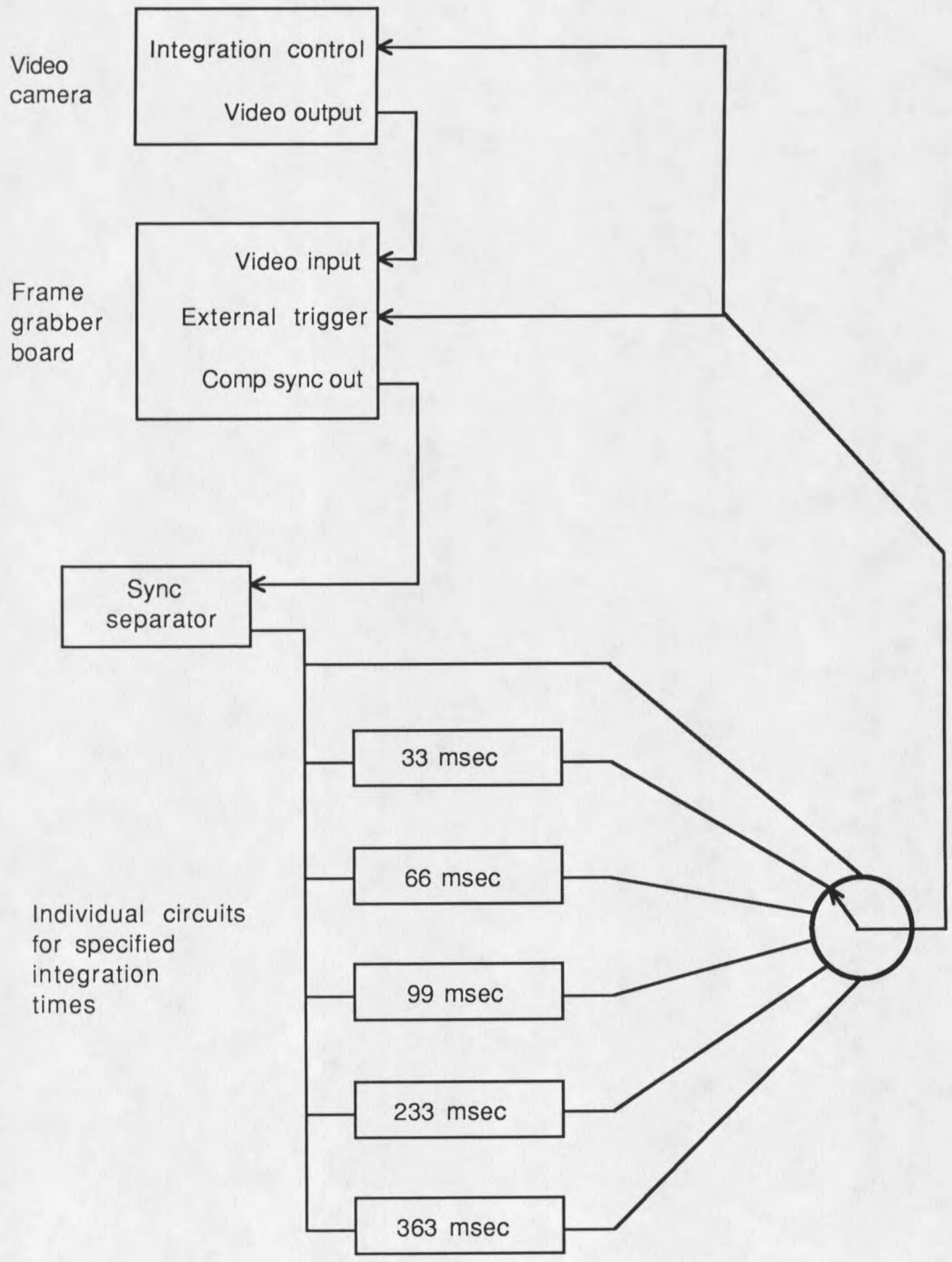

Figure 26: Block diagram for the video camera timing circuit

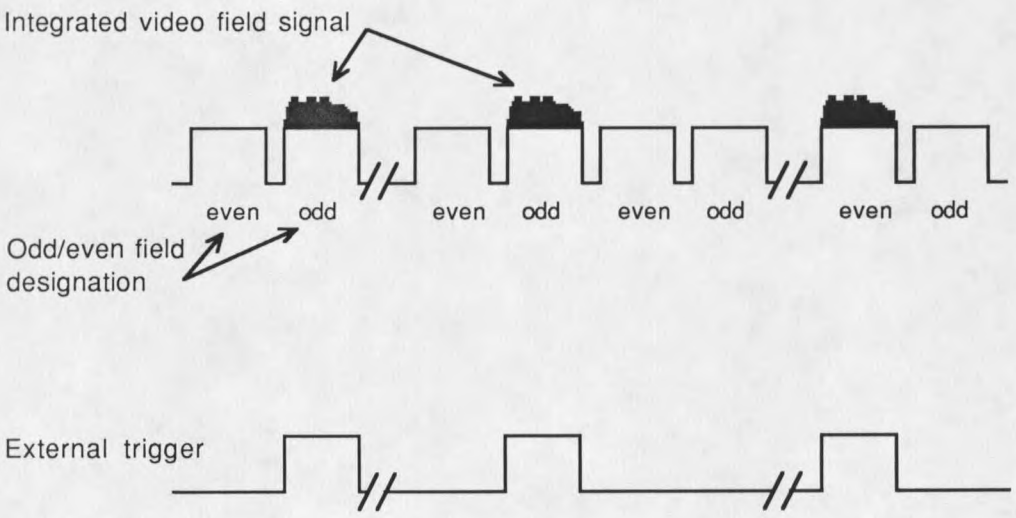

Figure 27: Integrated output and external trigger timing

REFERENCES

REFERENCES

1. E. Lendvay and others, J. Crystal Growth, 71(1985), 538.

2. C.B. Duke, in: Surface Properties of Electronic Materials, Chap. 3, eds. D.A. King and D.P. Woodruff, (Elsevier, 1988).

3. A. Kahn, Surf. Sci. Rep., 3(1983), 193.

4. T. Guo, R.E. Atkinson, and W.K. Ford, Phys. Rev. B (in press).

5. R.L. Park and H.H. Madden, Surf. Sci., 11(1968), 188.

6. E.A. Wood, J. Appl. Phys., 35(1964), 1306.

7. G. Ertl and J. Kuppers, Low Energy Electrons and Surface Chemistry, (VCH Verlagsgesellschaft, 1985).

8. M.A. Van Hove, W.H. Weinberg, and C.M. Chan, Low Energy Electron Diffraction, (Springer, 1986).

9. C.B. Duke, Adv. Chem. Phys., 27(1974), 1.

10. W.K. Ford, C.B. Duke, and A. Paton, Surf. Sci., 115(1982), 195.

11. N.W. Ashcroft and N. Mermin, Solid State Physics, (Holt, Rinehart, and Winstar, 1976).

12. J.J. Skauri, Modern Quantum Mechanics, (Addison-Wesley, 1985).

13. J.C. Slater, Phys. Rev., 81(1951), 385.

14. S. Hara, J. Phys. Soc. Japan, 22(1967), 710.

15. T. Guo, R.E. Atkinson, and W.K. Ford, Rev. Sci. Inst. (in press).

16. R.E. Atkinson, Baccalaureate Thesis, Dept. of Physics, Montana State University, (1988).

17. D. Briggs and M.P. Seah, Practical Surface Analysis by Auger and X-ray Photoelectron Spectroscopy, (John Wiley & Sons, 1983).

18. K.L. Chopra and I. Kaur, Thin Film Device Applications, (1983).

REFERENCES-continued

19. Sloan Technology Corporation, Santa Barbara, CA, Instruction Manual for Model DTM-200 Digital Thickness Monitor, 3rd Ed., (1973).

20. C.B. Duke, A. Paton, and A. Kahn, Phys. Rev. B, 27(1983), 3436.

21. J. Carelli and A. Kahn, Surf. Sci., 116(1982), 380.

22. M. Henzler, in: Electron Spectroscopy for Surface Analysis, Ed. M. Bach, (Springer, 1977).

23. W.K. Ford, T. Guo, S. Lantz, K. Wan, S.L. Chang, C.B. Duke, and D.L. Lessor, J. Vac. Sci. Tech. (in press).

24. A. Bowler, E.S. Hood, S.L. Chang, T. Guo, and W.K. Ford (unpublished).

25. P. Skeath, C.Y. Su, W.A. Harrison, I. Lindua, and W.E. Spicer, Phys. Rev. B, 27(1983), 6246.

26. C.B. Duke, A. Paton, W.K. Ford, A. Kahn, and J. Carelli, Phys. Rev. B, 26(1982), 803.

27. J.A. Nelder and R. Meade, Comp. J., 7(1965), 308.

28. Numerical Recipes by Press, et.al.

29. M.S. Cacecci and W.P. Cacheris, Byte, May 1984, 340.